# Impact of North American intense fires on aerosol optical properties measured over the European Arctic in July 2015

**K.M. Markowicz[1], P. Pakszys[2], C. Ritter[3], T. Zielinski[2], R. Udisti[4], D. Cappelletti[5], M. Mazzola[6], M. Shiobara[7], P. Lynch[8], O. Zawadzka[1], J. Lisok[1], T. Petelski[2], P. Makuch[2], G. Karasiński[9]**

[1]Institute of Geophysics, Faculty of Physics, University of Warsaw, Warsaw, 02-093, Poland

[2]Institute of Oceanology, Polish Academy of Sciences, Sopot, 81-712, Poland

[3]Alfred Wegener Institute, Helmholtz Centre for Polar and Marine Research, Potsdam, 14473, Germany

[4]Department of Chemistry - Analytical Chemistry Section, University of Florence, Florence, I-50019, Italy

[5]Department of Chemistry, Biology and Biochemistry - University of Perugia, Perugia, I-06123, Italy

[6]ISAC-CNR, Bologna, Italy

[7]National Institute of Polar Research, Tokyo (NIPR)

[8]Naval Research Laboratory, Marine Meteorology Division, Monterey, USA

[9]Institute of Geophysics Polish Academy of Sciences, 01-452 Warsaw, Poland

Corresponding author: Tymon Zielinski (tymon@iopan.gda.pl)

**Key points:**

- Extreme air pollution in the European Arctic studied in summer 2015
- Biomass burning event in North America led to aerosol optical depth of more than 1 at 500 nm
- This biomass burning was observed mostly in middle and lower troposphere but also in the lower stratosphere

**Abstract**

In this paper impact of intensive biomass burning (BB) in North America in July 2015, on aerosol optical and microphysical properties measured in the European Arctic is discussed. This study was made within the framework of the Impact of Absorbing Aerosols on radiating forcing in the European Arctic (iAREA) project. During the BB event aerosol optical depth (AOD) at 500 nm exceeded 1.2 in Spitsbergen and 0.7 in Andenes (Norway). Ångström Exponent (AE) exceeded 1.4 while the absorbing Ångström Exponent (AAE) varied between 1 and 1.25. BB aerosols were observed in humid atmosphere with a total water vapor column between 2 and 2.5 cm. In such conditions aerosols are activated and may produce clouds at different altitudes. Vertical structure of aerosol plumes over Svalbard, obtained from ceilometers and lidars, shows variability of range corrected signal between surface and middle and upper troposphere. Aerosol backscattering coefficients show values up to $10^{-5}$ $m^{-1}sr^{-1}$ at 532 nm. Aerosol surface observations indicate chemical composition typical for biomass burning particles and very high single scattering properties. Scattering and absorption coefficients at 530 nm were up to 130 and 15 $Mm^{-1}$, respectively. Single scattering albedo at the surface varied from 0.9 to 0.94. The averaged values over the entire atmospheric column, ranged from 0.93 to 0.99. Preliminary statistics of model and sunphotometer data as well as previous studies indicate that this event, in the Arctic region, must be considered extreme (such AOD was not observed in Svalbard since 2005) with a significant impact on energy budget.

## 1. Introduction

The climate is a primary driving force of fire activity both globally and on a regional scale (Tosca et al., 2013). However, fires influence climate on similar temporal and spatial scales by means of emissions of trace gases and aerosols (Marlon et al., 2008; Power et al., 2008; Bowman et al., 2009; Ward et al. 2012). Numbers of large biomass burning (BB) events have been gradually increasing over the last 100 years and anthropogenic activities are the main factor in this process, which can be related both to climate changes and agricultural

climate warming over the last several decades has significantly increased the number of large wild fires in North America (Westerling et al., 2006; Turetsky et al., 2011). Satellite observations of burned areas and active-fire thermal anomalies provide evidence that the El Niño–Southern Oscillation and other climate factors also modify fire activity in various ecosystems, including tropical forests and savanna ecosystems (Spessa et al., 2005; van der Werf et al., 2010; Field et al., 2009; Fernandes et al., 2011; Chen et al., 2011).

BB aerosols include a great variety of carbonaceous substances characterized by a variable carbon oxidation state with different optical properties. Thermally refractory (elemental) carbon is mostly responsible for absorption of solar radiation. This carbonaceous fraction of aerosols is typically defined as black carbon (BC), based on its optical properties, or elemental carbon (EC), operationally determined with thermo-optical measurements. Organic carbon (OC), being more complex from a chemical point of view, shows more complex optical behavior. Specifically, OC may lead both to wavelength dependent radiation scattering (Cooke and Wilson, 1996; Haywood and Ramaswamy, 1998; Liousse et al., 1996) and absorption (Andreae and Gelencser, 2006) in the generic form of brown carbon, BrC, introduced to distinguish all the organic substances absorbing light and appearing brown rather than black. Apart from these definitions being usually not congruent and sometimes confusing, it is clear that BB aerosols have a significant impact on the climate system (IPCC, 2013). However, the quantitative estimate of BB radiation effect is complex (Wang et al., 2007).

Atmospheric aerosols are responsible for the modification of the energy budget of the surface, and they affect the climate both locally (Ramanathan et al., 2001) and globally. However, as the IPCC reports (www.ipcc.ch) show, uncertainties are still significant regarding their radiative and climate effects (IPCC, 2007; IPCC, 2013). Aerosol particles, including those from BB, due to their scattering and absorptive properties, are responsible for a number of environmental effects, i.e. they play a major role in the reduction of visibility, and they can also have a significant impact on incoming UV radiation on the Earth's surface (Torres et al., 1998, 2007), and on photochemistry in the boundary layer (BL) (Graber and Rudich, 2006; Kirchstetter et al., 2004).

The most recent IPCC report indicates a BB radiative forcing (RF) of –0.01 ± 0.08 W/m$^2$ following the results of AeroComII 28 models (Myhre et al., 2013). However, previous results showed the global annual mean direct RF of BB of about 0.03±0.12 W/m$^2$ (Forster et al., 2007). This result of nearly zero BB radiative forcing is a result of the compensation of a strongly positive BC radiative forcing by a negative one from organic aerosols (Myhre et al., 2013). The estimates reported by Bond et al. (2013) for the period from 1750 to 2005, show direct radiative forcing of atmospheric BC at +0.71 W/m$^2$ with 90% uncertainty bounds of (+0.08, +1.27) W/ m$^2$. However, according to Bond et al. (2013) the total direct forcing of BC from all known sources, with the pre-1750 background included, has been estimated at a level of +0.88 (+0.17, +1.48) W/ m$^2$. Bond et al. (2013) also reported that: "the best estimate of industrial-era climate forcing of BC through all forcing mechanisms, including clouds and cryosphere forcing, is +1.1 W/ m$^2$ with 90% uncertainty bounds of +0.17 to +2.1 W/m$^2$." Although, the global mean of BB radiative forcing is small, the magnitude of some regional BB radiative forcing is two to three times larger. Such a strong direct radiative forcing of BB aerosols over the emission source region may play a significant role in regional and global climate. The Arctic climate system is very sensitive to climate changes due to the ice-albedo feedback mechanism (Screen and Simmonds, 2010). The climate of the Polar regions is partly tuned by atmospheric aerosols, since they affect the distribution of radiation, which reaches the surface.

While the majority of pollution in the Arctic originates from more southerly latitudes, local sources are limited to the area of the Arctic Circle (Law and Stohl, 2007). Long-range transport of aerosols is greatest in winter and spring, when the southward shift of the Arctic front facilitates the advection of polluted air from mid-latitudes. Natural particles (sea salt and mineral dust) are an important source of aerosols in the Arctic. Both aerosol types contribute up to 50% to the total particle mass at the surface (Tomasi et al., 2012). In the last decade, in some years (2005, 2006, 2008 and 2011) high values of Aerosol Optical Depth (AOD), ranging from 0.3 to even 0.8, were observed due to strong spring aerosol events such, as the Arctic Haze or the advected pollution from BB sources (Pakszys et al., 2015). The relatively high AOD, which may indicate the presence of larger scale atmospheric pollution

In this paper the authors describe a biomass burning episode from the summer of 2015, studied during the one of the iAREA (Impact of Absorbing aerosols on Radiative forcing in the European Arctic) campaigns, and its consequences for the aerosol load over the European Arctic. The iAREA project (http://www.igf.fuw.edu.pl/iAREA) has been founded by the Polish-Norwegian Research Programme for a period between 2013 and 2016. The main motivation for the studies described in the paper is to quantify the aerosol optical and microphysical properties during the most intensive BB event in the European Arctic since 2005 (when the AERONET station in Hornsund was established). Results of this research will be used in frame of the iAREA project to estimate the impact of the event on the radiation budget in European Arctic as well as for modification of thermodynamics processes in the lower troposphere related to absorbing particles.

The wild fires, analyzed by the authors, occurred in North America in July 2015. According to the Global News Canada, 2015 was one of the worst years within the last 5 years in terms of the number of forest fires. Natural Resources Canada reported that 2015, from many statistics, appeared as the worst in 5 years (http://www.nrcan.gc.ca). For example, the area of land burned in 2015 was larger in 6 out of 10 provinces, when compared with the last ten years. In number, this means 3,953,000 hectares of burned land in 2015 versus 2,090,000 hectares as an average of the last decade (Canadian Wildland Fire Information System; http://cwfis.cfs.nrcan.gc.ca).

The overview of research stations and measurement platforms is presented in Section 2. In Section 3 we describe the methodology, including instrumentation and models. Section 4 provides information on large scale AOD spatial distribution (Subsection 4.1), BB source regions (Subsection 4.2), comparison of remote sensing aerosol optical properties including transport from the HYSPLIT model (Subsection 4.3), and in-situ optical and microphysical properties (Subsection 4.4). Finally, conclusions are drawn in the last section.

## 2. Study sites description

During the iAREA campaign, both in-situ and sunphotometer aerosol measurements were carried out in Andenes, Hornsund, Ny-Ålesund, and onboard of the r/v Oceania (Figure

800 m from the south-west of Ny-Ålesund research village and by the Zeppelin station (78.908°N, 11.881°E, 474 m a.s.l.). The aerosol remote sensing observation was carried out at the French-German Arctic Research Base AWIPEV (Alfred Wegener Institute and Polar Institute Paul Emile Victor) and the Japanese station belonging to the National Institute for Polar Research.

The Polish Polar Station in Hornsund is located in the southern part of Spitsbergen (77.00° N, 13.55° E, 12 m a.s.l.), in the bay of Isbjørnhamm in the Hornsund fjord, the largest southernmost fjord on Svalbard (Figure 1). This reference site (with the lack of local anthropogenic emissions) is surrounded by a bay from the south side, and by mountains from the other three sides (up to 700 m a.s.l.), with the Hans Glacier on the east side. The mountains are aligned longitudinally and coastal plains dominate the landscape.

Norwegian Arctic Lidar Observatory for Middle Atmosphere Research (ALOMAR), the southernmost station during the 2015 campaign, is located on the west coast of northern Norway, on the northernmost island – Andøya of the Vesterålen archipelago, situated about 300 kilometers inside the Arctic circle (Figure 1). The ALOMAR observatory is located at the top of the mountain at 380 m a.s.l. (69.279°N, 16.009°E).

The in-situ aerosol data were collected during the Arctic cruise of the r/v Oceania to the Greenland Sea. The cruise route during the biomass burning event is shown in Figure 1. The r/v/ Oceania belongs to the Institute of Oceanology Polish Academy of Sciences. Every year the operational area routinely covers the Baltic Sea, the European Arctic Seas and the Spitsbergen Fjords.

## 3. Instrumentation and models

### 3.1. Sunphotometers

Aerosol Optical Depth (AOD) and Ångström Exponent (AE) data were obtained from the Microtops II sunphotometer measurements (in Hornsund) produced by the Solar Light Company, and CIMEL sunphotometers (Polish Polar Station and the ALOMAR observatory in Andenes). The Polish Polar Station and the ALOMAR sunphotometers belong to the

Single measurement "shots" were acquired over periods of about 1 minute. Measurements were made at five wavelengths (440, 500, 675, 870, 1020 nm), 10 seconds per channel approximately every 20 minutes. In order to reduce potential sun pointing error, five scans were performed with each measurement and the scan with the smallest standard deviation was used in data processing. The improvement of data quality involved the elimination of cloud contamination, the visual inspection of sky conditions during the measurements and the analysis of satellite images, which were done for each Microtops observation. Calibration of the Microtops II was done in June 2015 to the CIMEL sunphotometer at the Strzyzow AERONET station in accordance to the procedure described by Bovchaliuk et al., (2013).

For further analyses, the authors used level 1.5 (cloud-screened) data from the ALOMAR AERONET station since level 2.0 data was available only from the Hornsund station. Level 1.5 data do not include control of the quality and the final calibration. The calibration coefficients in this case were taken from the pre deployment calibration. For the level 2.0 data, the post deployment calibrations were also taken into account. In case of small detector degradation and in clean Arctic conditions (clean optics), the temporal variation of the calibration coefficient is very small. The uncertainty of the AOD (level 2.0) retrieval from the CIMEL measurements is ±0.01 (Eck et al., 1999) and from the Microtops II, it does not exceed ±0.02 (Knobelspiesse et al., 2004). For the level 1.5 AOD, the uncertainty is difficult to estimate but can range from ±0.01 to ±0.05 for an air mass of 1 (which means sun in zenith). In case of the AE, the uncertainty decreases significantly with the AOD and for a very high AOD (1.0 at 500 nm), it is less than ±0.06 (Zawadzka et al., 2013).

In Ny-Ålesund AOD and AE, as well as precipitable water (PW) measurements were obtained with the fully automatic sun photometer SP1A (Table 1) produced by Dr. Schulz and Partner GmbH (http://www.drschulz.com/cnt/). The SP1A sunphotometer measures direct solar radiation at 10 channels ranging between 369 nm and 1023 nm with a field of view of 1˚ (Herber et al., 2002). The measured signal is temperature corrected with an operating temperature range of -30 $^{o}$C to 40 $^{o}$C. Langley methodology for the instrument calibration is performed every year in pristine mountainous areas such as Spain or Tenerife.

### 3.2. Lidars and ceilometers

In this study, we used data from three lidars and two ceilometers. The Koldewey Aerosol Raman Lidar (KARL) (Table 1) in Ny-Ålesund measures the backscatter coefficient at 355, 532, 1064 nm, as well as the extinction coefficient and depolarization at 355 and 532 nm. It consists of a 70 cm detection mirror, working with a field of view of approximately 2 mrad and a 50 Hz Nd:YAG laser which emits about 10 W for each of the three wavelengths. Technical parameters and data analysis techniques have been described by Hoffmann (2011) and Ritter et al., (2016). Uncertainties of the aerosol backscatter coefficients' retrieval at 355 nm and 532 nm are up to 5% and up to 10% at 1064 nm, while the error for the aerosol extinction coefficient at about 5 km altitude for this data is around 50% at 355 nm and 100% (meaning the error is as large as the extinction value) at 532 nm (Ritter et al., 2016). Above 5 km altitude only the backscatter was considered.

During the study period, additional measurements were made using the Micro Pulse Lidar (MPL) from the Micro-Pulse Lidar Network (MPLNET) (http://mplnet.gsfc.nasa.gov) located at the station in Ny-Ålesund (Campbell et al., 2002). The MPL lidar measures the backscattering coefficient at 523 nm wavelength with 1-minute resolution. It uses the Nd:YLF laser diode with a pulse frequency of 2500 Hz 100 mrad and a field of view resulting in vertical profiles ranging 60 km with 30 m resolution (Spinhirne et al., 1995).

At the Polish Polar Station in Hornsund, aerosol observations were made with use of the Raman lidar with a 330 mm Newtonian telescope (Pietruczuk and Karasinski, 2010). As a light source, pulsed Nd:YAG laser simultaneously emits light at three wavelengths (1064, 532 and 355 nm) in pulse duration of 7 ns with pulse energy of 300, 240 and 160 mJ, respectively. Additionally, light at 386 and 407 nm is detected. These channels correspond to inelastic (Raman) scattering of 355 nm wavelength on $N_2$ and $H_2O$ molecules, respectively. Detection of weak Raman scattering is possible only during night due to sun light dazzle of sensitive photon counting detectors. The lidar sounds the atmosphere vertically twice a day for 2 hours with respect to weather conditions and cloudiness. The vertical resolution is 15 m and integration time is 20 s. The overlap point is located at above 2 km a.s.l..

In addition, the authors used data from the CL51 Vaisala Ceilometer

The Lufft (http://lufft.com) CHM15K "Nimbus" (Table 1), similarly to CL51, measures cloud height, boundary layer height and visibility within the lowermost atmospheric layer of 15 km (Wiegner et al., 2014; Madonna et al., 2015). CHM15K uses a diode-pumped Nd-YAG laser (1064 nm) yielding about 8 µJ per pulse at a 5-7 KHz repetition rate. Further details on the CHM15K ceilometers are described by Flentje et al. (2010) and Frey et al. (2010).

### 3.3. In-situ aerosol equipment

Aerosol scattering properties were measured using TSI nephelometer 3563 (onboard r/v Oceania) operating at 3 wavelengths with 1-minute resolution (Anderson et al., 1996). Data from the nephelometer were corrected for angular non-Lambertian illumination and for truncation error based on the methodology described by Anderson et al., (1996) and Anderson and Ogren, (1998). The uncertainty of the aerosol scattering coefficient due to both effects is about 3% for single scattering albedo larger than 0.8. For very low single scattering albedo the uncertainties are much higher and reach about 30% at single scattering albedo of 0.4 (Massoli et al., 2009). Several previous studies (e.g. Heintzenberg et al., 2006) have estimated total uncertainty of scattering coefficient measurement of the TSI nephelometer at around 10%. In Ny-Ålesund a single wavelength (530 nm) Radiance Research M903 Nephelometer (Müller et al., 2009) was used to measure aerosol scattering coefficient.

A Magee aethalometer AE-31 was used to measure BC concentration (at the Zeppelin station and onboard the r/v Oceania). The aethalometer measures the transmission through a quartz filter over a wide spectrum of wavelengths, in our case between 370 and 950 nm. A change in filter attenuation is then translated to the mass concentration of BC particles. In case of AE-31 instruments, the data must be corrected for filter non-linear loading effects and for multiple scattering which leads to the enhancement of light absorption by particles in the filter matrix. For this purpose, the authors used the methodology described by Segura et al., (2014). The uncertainty of BC concentration is about 8% (Eleftheriadis et al., 2009).

BC concentration and absorption coefficients were measured by a Radiance Research Particle Soot Absorption Photometer (PSAP) (Table 1). The PSAP, similar to the Magge

Research M903 Nephelometer (Müller et al., 2009), and aerosol size distribution recorded in the ranges 10-487 nm and 523 nm – 20 μm by a TSI Scanning Mobility Particle Sizer (SMPS) and by an Aerosol Particle Sizer (APS), respectively. The SMPS and APS instruments were certified by the manufacturer. The calibration system meets the ISO–9001:2000 certification requirements, the Quality Management Systems Requirements and complies with the ISO 10012:2003 and Quality Assurance Requirements for Measuring Equipment. A typical single channel uncertainties in aerosol number distribution, in case of the SMPS and APS, are 20% and 18%, respectively (Buonanno et al., 2009).

In addition, aerosol samples were continuously collected with a TCR TECORA SkyPost Sequential Sampler. $PM_{10}$ (particle matter with a 10 μm cut–off head) data were collected daily (00:01 – 23:59 UTC) on Teflon filters (Pall, 47 mm diameter, 2 μm nominal porosity) mounted on a Dekati $PM_{10}$ 4-stage Impactor (>10, 10-2.5, 2.5-1, < 1 μm). The sampling head was designed according to EN–12341 European standard and operated at a flow rate of 38.3 L $min^{-1}$ (actual volume), corresponding to a 24 h volume of about 55 $m^3$. Levels of cations ($Na^+$, $K^+$, and $Ca^{2+}$) were determined using a Dionex CS12A–4 mm analytical column with a 20 mM $H_2SO_4$ eluent. Level of inorganic anions ($SO_4^{2}$) were measured by a Dionex AS4A–4 mm analytical column with a 1.8 mM $Na_2CO_3$ / 1.7 mM $NaHCO_3$ eluent. Reproducibility of iron chromatography data is better than 2% for all the components (Morganti et al., 2007) while uncertainties are below 5%. The inlet for all in-situ instruments was about 3 m a.g.l. at Gruevebadet and about 8 m a.s.l onboard the r/v Oceania. For Zeppelin station, the authors used AE-31 based observation of BC concentration for the last 12 years.

### 3.4. Radiation instruments

Radiation flux data were obtained from the BSRN (Baseline Surface Radiation Network) facility in Ny-Ålesund. Direct solar flux is measured by a Kipp & Zonen CHP1 pyrheliometer on a Schulz&Partner solar tracker shared with the diffuse radiation measurement by a ball-shaded Kipp & Zonen CMP22. Total incoming and reflected solar radiation is also measured by CMP22 instruments, while upward and downward longwave

### 3.5. Aerosol transport models

The Navy Aerosol Analysis and Prediction System (NAAPS) model (Witek, et al., 2007) was used to assess the spatial distribution of the aerosol concentration and optical properties. A decadal long global 1x1 degree and 6-hourly 550 nm AOD reanalysis product was recently developed and validated at the Naval Research Laboratory (Lynch et al., 2016). This reanalysis utilizes a modified version of the NAAPS as its core and assimilates quality controlled retrievals of AOD from MODIS on Terra and Aqua and the Multi-angle Imaging SpectroRadiometer (MISR) on Terra (Zhang et al., 2006; Hyer et al., 2011; Shi et al., 2014). The reanalysis version of the NAAPS is driven by the Navy Operational Global Analysis and Prediction System (NOGAPS; Hogan and Rosmond, 1991). The NAAPS characterizes anthropogenic and biogenic fine particles (ABF, including sulfate, and primary and secondary organic aerosols), as well as, dust, biomass burning smoke and sea salt aerosols. Aerosol source functions and removal processes were regionally tuned. Smoke from biomass burning was derived from near-real time satellite based on thermal anomaly data used to construct smoke source functions as in the Fire Locating and Modeling of Burning Emissions (FLAMBE1.0; Reid et al., 2009).

Previous studies indicate that FLAMBE emission has the best performance in South America, where the correlation coefficient between the model and AERONET AOD is between 0.75 and 0.83 (Reid et al., 2009). However, in Boreal regions, NAAPS shows mixed results. FLAMBE detects and properly models transport of significant boreal fires but there is a difficulty with emission magnitudes for individual events. Reid et al., (2009) showed that FLAMBE underestimates AOD by a factor of 2-3 and the correlation coefficient between the measured and modeled AOD is in the range of 0.26-0.49. Including the assimilation of AOD from MODIS observations significantly increases the consistency between the model and the NAAPS AOD.

However slightly different from the FLAMBE1.0, a two-day maximum (previous day and present day) fire signal was used to mitigate missing detections of fires by unavailable orbital coverage and thick clouds. Regional multipliers on smoke emission were then applied based on the comparisons between the natural model (no AOD data assimilation) AOD and

biomass burning smoke. Lynch et al., (2016) reports some long-term (2003-2013) statistics between the NAAPS and the AERONET derived AODs for North America boreal region. Between December and May mean bias, root mean square error and the square of the Pearson correlation coefficient is 0.02, 0.05 and 0.47, respectively. The same parameters between July and November are 0.01, 0.08 and 0.64. For comparison, the global mean bias, root means square error and the square correlation coefficient is 0.01 0.14 and 0.67 for the first period and 0.01, 0.14 and 0.71 for the second one.

### 3.6. Satellite data

The results of ground-based observations were supported by analyses of the satellite AOD data obtained from MODIS, mounted onboard the Aqua and Terra satellites. Data from level 2 of the MOD04_L2 (Terra) and MYD04_L2 (Aqua) products of the 06 collection were used (Levy et al., 2013). Basic satellite data were averaged for each day and gridded to a 10x10 km spatial resolution. In addition, to minimize errors relating to high optical air-mass, only data collected at a satellite zenith angle of less than 60° have also been taken into account. According to Levy et al., (2013) the AOD uncertainty from the MODIS retrieval is ± (0.05 + 15 %) over land and ((+(0.04 + 10 %), −(0.02 + 10 %)) over the ocean.

### 3.7. Backward trajectories model

In order to distinguish the sources of inflow of air masses, backward trajectories of air advection were modelled with the use of the NOAA HYSPLIT model (HYbrid Single-Particle Lagrangian Integrated Trajectory Model) (Draxler et al., 1997) using the NCEP/NCAR Reanalysis (1948 - present). Each trajectory was calculated for 144 hours, starting at 00:00 UTC at two locations: north Spitsbergen close to Ny-Ålesund, and the Andenes area. For this purpose we used the trajectory ensemble option. Each member of the trajectory ensemble is calculated by offsetting the meteorological data.

## 4. Results and discussion

This section includes the results of the spatial distribution of AOD from satellite (MODIS) observations and the NAAPS simulation during the BB event. Next, the data from

**4.1. Spatial distribution of AOD from MODIS and NAAPS**

To provide spatial information about the AOD over the study region, all available MODIS images of AOD over the Arctic for the period between 10 and 13 July, 2015 were analyzed. Unfortunately, that period of July was rather cloudy in the study area, which resulted in a set of spatially scattered satellite data. The MODIS derived AOD for the period between 10 and 13 July 2015 over the study region are presented in Figure 2. The measurement stations are denoted with red dots. The MODIS data show a significant increase of AOD around Spitsbergen on 10 July 2015. The AOD reached a level of up to 0.7 west from Spitsbergen. According to Figure 2, MODIS AOD at Andenes was higher (up to 0.7) on the 12$^{th}$, compared to 0.4-0.5 on the 11$^{th}$. Patches of high AOD value(Figure 2c.: 0.6 at 550 nm) were still observed on those two days south of Svalbard.

The reanalysis of a 6-hour NAAPS smoke AOD (in polar projection) for the European Arctic showed enhanced concentrations of smoke (Figure 3) at 18:00 UTC between 5 and 12 July, 2015.

The NAAPS model clearly shows a lot of BB particles in high-latitudes. The projections for each of the 8 days show AOD of smoke plumes above 1.0 (at 500 nm) over Canada and Alaska. Some evidence of smoke particles is simulated also over the Siberia. The significant increase of AOD around the Canada–United States border and close to the eastern part of North America's coasts is clearly connected with the presence of the smoke particles in the air due to intensive smoke fire emissions in southern and central Canada. The smoke reached Greenland coast on 7-11 July, 2015. The BB plumes emitted over Alaska moved in the northwest direction over the East Siberian Sea (Figure 3b-d) and next over the Arctic Ocean (Figure 3d-e). The BB has reached the Spitsbergen region around 18 UTC on 9 July (Figure 3e) then on two subsequent days it had spread to Norway, reaching Andenes (Figure 3g-h). To better understand the movement of the aerosol plume, see the NAAPS animation in the supplementary material. The maximum of BB AOD simulated by NAAPS over Spitsbergen was around 0.6 (18 UTC, 10 July). More details about the BB event

total AOD is about 60-75%. In case of Andenes plumes are simulated 2 days later and are less intensive. The smoke AOD reached the level 0.2 while in Hornsund and in Alesund 0.4 and 0.6, respectively.



**4.2. Fire biomass burning sources**

According to the Terra and Aqua fire data obtained from the FIRMS MODIS Active Fire Data service (https://firms.modaps.eosdis.nasa.gov/firemap/) and the Canadian Wildland Fire Information System (http://cwfis.cfs.nrcan.gc.ca), the main fire regions during the period between 28 June and 5 July 2015 were found to be situated in the central part of Canada, in provinces of British Columbia, Alberta and Saskatchewan. The fire episode started in late May and early June 2015 within the area surrounding Lake Athabasca. The fire further developed to affect a greater part of Canadian territory. The culmination of the fire was observed on 28 June, 2015. The peak of the fire activity lasted for 3 subsequent days, during which the fire area was extended towards the north, passing almost the entire territory of Canada. The fire spots were observed in the region about 100 km south-west from the Great Bear Lake and ending 200 km north-west of Winnipeg Lake. Since 1 July 2015, the area covered by fires had been gradually shrinking, and it had mostly surrounded the Reindeer and Athabasca Lakes. The intensive fire period finished around 15 July 2015. Nevertheless, the increased fire activity in the Canadian region continued throughout July and a part of August 2015. This is best well seen in the plots of the Fire Weather Index (FWI), a numeric rating of fire intensity (Figure 5).

According to reports prepared by the Alaska Interagency Coordination Center – fire spots were existing continuously from mid May to late Jul 2015 affecting area of almost 21 000 $km^2$ (http://fire.ak.blm.gov/predsvcs/intel.php; day of access: 14.09.2016). At the beginning of the period most of fires were caused by the human activity - around 250 individual spots were registered at the eastern part of Alaska Range Mts. and the valley of Kuskokwim River (MCD14ML MODIS product, coll. 5.1). Nevertheless, the most significant period for this study began between 19 – 25 of June, where up to 300 new fire spots appeared being mainly introduced by lightning strikes (Figure 6).

of biomass burning plume most probably between 4 and 6 July 2015 (see also section 4.3 with back trajectories analysis).

Subsequently, a single map of land coverage was obtained from the MCD120C1 MODIS product, which contains annual distribution of 17 land cover classes based on the International Geosphere Biosphere Programme classification (Loveland and Belward, 1997). We used the most recent available data from 2012 assuming no significant changes. The latter was intersected with fire spot locations in Alaska indicating tundra to be the predominant type of burned vegetation (91%), however consisting of two subclasses: open shrublands, determining 52% of burned area and shrublands with sparsely located trees (39%).

**4.3. Comparison of aerosol optical properties at three measurement stations**

As presented in Figures 3 and 4, the smoke plume first reached the station in Ny-Ålesund in the afternoon of 9 July. This station is the northernmost station of all the three stations discussed. Figure 7 shows temporal variability of AOD at 500 nm and the AE based on the 440/870 nm AOD measured with sunphotometers at all three stations between 9 and 16 July 2015. Data from the r/v Oceania were not available because of cloud conditions during that period. Taking into consideration potential measurement errors due to the presence of cirrus clouds, an algorithm developed by Alexandrov et al., (2004) was used for cloud screening of the sunphotometer data.

Smoke plumes reached Andenes on before midnight 11 July 2015. Relatively smaller AODs (around 0.4) compared to Svalbard values are consistent with the gradual reduction of the smoke component, as seen from the MODIS images. With increasing AOD values on 9 July over Spitsbergen, values of the AE simultaneously increased which is related to the decrease of particle sizes. This reduction of sizes confirms the presence of small smoke aerosol particles in the atmosphere. The peak of the AOD value of more than 1 was observed on 10 July 2015 in Ny-Ålesund with very high values (about 0.9) and slightly lower values (about 0.7) that were recorded in Hornsund using the CIMEL and the Microtops II

the period between 9 and 15 July 2015 the AOD values clearly fluctuated, i.e. on 10 July the AOD values changed from 0.3 to 1.5 and then to 0.5 during the day over Ny-Ålesund, which confirms that smoke particles advected the study areas in a form of plumes.

During the entire smoke event all AE values exceeded 1 (average about 1.5), thus indicating fine particle dominance in the atmosphere at all sites. It is worth noting that the long-term (2005-2015) mean AE value for the Horunsund station was 1.29 (http://aeronet.gsfc.nasa.gov/). In comparison with the MODIS and NAAPS results, the sunphotometer observation shows lower values of AOD. For example, the MODIS maximum daily mean for 10 July (Figure 2a). was 0.7 at 550 nm, the NAAPS was about 0.8 at 550 nm (Figure 4a), while the in-situ daily AOD mean was about 0.8 at 500 nm (Figure 7a). Nevertheless, even the incomplete and slightly underestimated MODIS derived AODs confirm that the BB resulted in the transport of large amounts of smoke particles over the Arctic and during the study period it travelled across the Arctic reaching northern Europe.

AOD values 10-15 times higher than the typical values of that region, measured with use of sunphotometers, yield an attenuation of light as if a cloud was present. Indeed, we found that the BB aerosol event was so thick that in Ny-Ålesund the CL51 missed high altitude clouds at least once. Figure 8 presents a logarithm of the CL51 ceilometer range corrected signal measured in Ny-Ålesund between 9 and 12 July 2015. The white color shows cloud layers while green and blue colors correspond to aerosol layers. However, the thresholds of the range corrected signal, which was used to distinguish cloud and aerosol particles, is assumed arbitrary and may produce some misclassification of aerosol or cloud layers. In addition, black dots in Figure 8 show the AOD measured by SP1A sunphotometers. Cloud conditions reported from the measurements taken with the use of the CL51 in Ny-Ålesund were more favorable than the sunphotometer observations. Some clouds were observed during the morning of 9 July 2015 (Figure 8) and during the afternoon of 10 July 2015. The CL51 ceilometer results show a clear sky with some aerosols in the Planetary Boundary Layer (PBL) and also in the middle troposphere. Some aerosol layers ranging between 3.5 and 6 km a.s.l. were visible before and after midnight on 9/10 July 2015.

A similar plot but for the Hornsund data, based on the CHM15K ceilometer and the CIMEL sunphotometer observations between 9 and 15 July 2015, is shown in Figure 9. For the Hornsund station, sunphotometer measurements on 10 July were performed during clear sky conditions (Figure 7a), where aerosol layers are visible between 1.5 and 5 km a.s.l. Cirrus clouds were, however, observed over Hornsund on 12 July 2015 (Figure 8) between 10.5 and 12 km a.s.l. During that day aerosol layers appeared between 3 and 4.5 km a.s.l., at around 6 km a.s.l. A relatively strong backscattering signal from these layers indicates a high extinction coefficient and a high optical depth of BB aerosols. Cirrus clouds in the zenithal direction were detected from ceilometer observation. However, the AOD retrieved from the CIMEL measurements after cloud screening (level 2.0 data) indicated a rather clear (no clouds) path between the surface and the sun direction. Some outstanding points in the time variability of the AE (Figure 7b) on 12 July may indicate that the AOD for this day was not fully cloud screened.

To support the statements above, range corrected signals from the measurements conducted with the use of the micro-pulse lidar (MPL) between 9 and 11 July, 2015 recorded at the Ny-Ålesund station, are presented in Figures 10 (a) - (c). A higher backscattering signal was observed between the afternoon of 9 July and at noontime of 11 July 2015 over Ny-Ålesund. The BB event probably lasted longer but low level clouds had prevented the lidar and sunphotometer observations. Aerosol layers on 9 July appeared between 3.5 and 6.5 km a.s.l but a very thin layer was also visible up to 8.5 km a.s.l. The lidar data show that the event started around 14:00 UTC which correlates very well with an increase in the AOD and AE values (Figures 10 (g) – (i)) obtained from the SP1A sunphotometer. However, the precipitable water (Figures 10 (g) – (i)) as well as the incoming longwave radiation (Figures 10 (d) – (f)) started to change around 2 hours earlier. It probably indicates that the change of the air masses over Ny-Ålesund started before the BB plume advection.

Lidar observations show that aerosol (green and yellow color) and cloud (pink and white) layers are mixed between 4 and 6 km a.s.l. This is far above the boundary layer altitude which, both from local radiosonde measurements at 11:00 UT and from the NCEP

aerosol event (compare Figures 10 (d) and (e)). On 10 July 2015 in the middle troposphere layer of the high lidar, range corrected signal lasted until 08:00 UTC while another aerosol structure appeared above the PBL at around 06:00 UTC. This layer was visible between 1 and 4 km a.s.l.. In addition, some of these aerosol layers were detected at up to 2 km a.s.l. before and after midnight of 9/10 July 2015. Also the lidar signal shows cloud contamination on 10 July, especially around noon. Cirrus clouds at about 10 km a.s.l. and middle level clouds were detected during the afternoon. Throughout 11 July residual layers of inflow air masses with smoke pollutants between the surface and the altitude of 3.5 km a.s.l. were also seen over Ny-Ålesund alongside some very thin, probably subvisual clouds at about 4-4.5 km a.s.l.

The impact of the BB aerosols (and clouds) on the incoming solar radiation is depicted in Figures 10 (d) – (f). The direct solar radiation from the BSRN (Baseline Surface Radiation Network) site in Ny-Ålesund was plotted in dark green color . AOD (500 nm), AE and precipitable water from the SP1A sunphotometer were plotted as black squares, red circles and blue squares, respectively. After the disappearance of clouds after 6:00 UTC on 9 July 2015 it was a clear day with a low AOD (0.05-0.1 at 500 nm) typical of the Arctic summertime. Around noon the surface received about 550 W/m$^2$ total and 500 W/m$^2$ direct shortwave radiation. However, starting at 14:00 UTC the atmosphere became more and more turbid, as the BB aerosols arrived. At the same time direct radiation decreased dramatically. For example, at 06:30 and 16:30 UTC the solar elevation was for both around 25$^o$. However, while in the morning in clear sky condition the direct radiation was about 400 W/m$^2$, with the solar elevation in the afternoon at an optical depth of around 0.5 at 500 nm, the direct radiation dropped by a factor of 2.

Measurements of the aerosol vertical structure were complemented with the use of the KARL lidar in Ny-Ålesund. An example of such results is provided in Figure 11. Also, in the KARL generated image from 10 July 2015 over Ny-Ålesund, the vertical profile of backscatter coefficient [m$^{-1}$sr$^{-1}$] shows the presence of some high altitude cirrus clouds above 10 km a.s.l. in the morning (not visible from the CL51 ceilometer). During the entire day very distinct aerosol layers were visible between 1 and 6 km a.s.l. with a backscattering coefficient

While comparing the backscatter contour plot of the lidar systems at Ny-Ålesund (Figure 11) to the range corrected lidar signal at the Hornsund station (Figure 13) some significant differences become evident. An undisturbed layered structure of increased backscatter at up to 3 km altitude and two shallow layers at up to 4 km altitude were seen above Hornsund. The temporal fluctuations of the lidar signal were, at least in the first hour of the measurements, very small. This seems to indicate an aerosol advection, which is not disturbed or modified by orography. The situation is different for Ny-Ålesund. Here, a higher temporal variation of the backscatter coefficient is obvious. The aerosol layer was also mostly defined in the lowest 4 km a.s.l., but appeared much more disturbed. At the station in Ny-Ålesund, aerosol layers were clearly visible up to 6 km (morning of 9 July) and 5 km in the evening. Such layers were not visible over Hornsund. Moreover, from the color ratio, which is a ratio of aerosol backscatter at 355 nm divided by 532 nm, clouds become evident through small values (Figure. 12). A Cirrus at 10-12 km altitude before noon is not our focus here, but a second cloud at 4-5 km altitude in the afternoon, i.e. altitude where formerly aerosols had been present, is visible. However, all other backscatter coefficients in Figure 11 are due to aerosol presence, even at altitudes, which by far, exceed the height of the Arctic boundary layer.

The notion that some aerosol reached the stratosphere and persisted there for at least one month is depicted in Figure 14. The backscatter coefficient from the AWI KARL lidar is plotted for a wavelength of 532 nm. A well-defined layer of an increased backscatter at an altitude of 10.5 km a.s.l. directly above the tropopause (c. 10.3 km at 11:00 UTC from the radiosonde on that day) can be seen. This layer only shows a weak aerosol depolarization of 1 - 2% which is far too small for cirrus clouds (Chen et al. 2002) and has a higher resemblance to stratospheric intrusions from forest fire aerosols (Fromm et al. 2008). The color ratio (ratio of aerosol backscattering coefficient at 355 and 532 nm) for this layer is 1.6, slightly larger than the rest of the stratosphere, while clouds tend to have a color ratio of around 1. The above presented results indicate that this layer consists of droplets of the size of the

Indirect retrieval from CIMEL measurements at Hornsund and Andenes stations provided information about columnar aerosol optical and microphysical properties. Mean daily values are presented in Table 2. All retrievals were made during AOD (440 nm)>0.4, which is recommended by Dubovik et al., (2000). The single scattering albedo (SSA) at 441 nm for Hornsund and Andenes stations was 0.98-0.99 and 0.93-0.94, respectively. According to Dubovik et al. (2000) the uncertainty of the SSA is ±0.03 indicating statistically significant difference between both stations. High SSA and low real part of refractive index on 10 July (1.35) in Hornsund may suggest that aerosols are strongly water soluble. However, on 12 July refractive index is much higher (1.49), while SSA indicates presence of non-absorbing particles. Imaginary index of refraction is one order of magnitude smaller in Hornsund in comparison to Andenes. For both stations the Absorbing Angstrom Exponent (AAE) is larger than AE which is consistent with decreasing of the SSA with change of wavelengths. Similar relation as well as the relatively high SSA has been reported by Markowicz et al., (2016) in Central Europe during the Canadian BB event in 2013. Also Eck et al., (2009) reported very week aerosol absorption, SSA ranging from ~ 0.96 to 0.97 at the Bonanza Creek AERONET station (Alaska) during boreal BB events in 2004 and 2005. In this case the SSA increases with altitude due to enhanced short wavelength absorption by organic carbon aerosols. High SSA values during the BB event result from small values of imaginary index of refraction, implying low black carbon fraction probably due to predominately smoldering combustion, coupled with large fine mode particle radius (Eck et al., 2009).

In order to determine the source of particles advected over Spitsbergen and northern Norway, air mass trajectories were calculated using the NOAA HYSPLIT MODEL with NCEP reanalysis data. Due to lack of meteorological observations in the Arctic, the trajectories become highly uncertain after around 5-6 days (Stock, 2010). For these reasons the authors present an ensemble of backward air mass trajectories, ending in Spitsbergen at 00:00 UTC between 10 and 12 July 2015 (Figure 15). The altitudes of the back trajectories over Ny-Ålesund were selected based on the aerosol layers detected using the lidars. For 10 July, altitudes of 2 and 6 km a.s.l. were selected for analyses, while for a period 11-12 July

within 4 to 6 days. Although the horizontal spread of back trajectories is not negligible transport of air masses from Alaska is very likely. However, on 11 and 12 July back trajectories ending at 2 and 4 km, show possible transport from different parts of Siberia. Vertical spread of the back trajectories is larger. Significant difference between back trajectory altitudes appears after 2-4 days. Therefore, initial altitudes of 6 day back trajectories are uncertain.

In case of Andenes the ensemble of back trajectories is more complicated (Figure 16). For example, on 13 July possible transport from Greenland and nethermost island of Canada at an elevation of 3 km was observed. A day before (Figure 16a) back trajectories are more consistent, indicating air mass transport from Alaska. This transport took place in the free and high troposphere and those air masses must have taken up aerosol from the widely spread forest fires that were blazing in this region. Further support for this statement is provided with information from the application of the NAAPS model (section 4.2).

**4.4. Optical and microphysical aerosol properties measured in Ny-Ålesund and onboard the r/v Oceania**

Figure 17 shows the results of in-situ surface observations plotted as hourly averages. The relative aerosol size distributions, as obtained at a 10-minute resolution from the SMPS and the APS measurements are presented in Figure 18. Between 9 and 16 July 2015 a significant increase of extensive aerosol optical properties (e.g. absorption, scattering and backscattering coefficients, and AOD) as well as a particle number concentration had been observed. At the peak of the event (11 July) surface aerosol scattering and absorbing coefficients exceeded an extremely high value of 130 and 15 $Mm^{-1}$ for 530 nm. Typical scattering coefficient in Ny-Ålesund is below 10 $Mm^{-1}$ while the absorbing coefficient is below 1 $Mm^{-1}$ (Lisok et al., 2016). SSA values were relatively constant and varied between 0.90 and 0.94 indicating moderate absorbing particles.

In addition, the AAE, measured for wavelengths 467 and 660 nm, was about 1 with some increase up to 1.4 during the BB event. Liu et al., (2014) reports that low absorption AE

is consistent with the characteristics of the BB event and possibly related to an aging and growing of the soot particles by their coagulation during transport and also to a hygroscopic growth near the ground due to very high relative humidity (Kotchenruther and Hobbs, 1998; Reid et al., 2005). The event at the surface was detected about 10 - 12 hours after its detection in the mid troposphere (see Figure 10a). The lidar and ceilometer data show that the event at the surface was less intensive than in the middle troposphere. The SMPS plots show some high particle concentrations in the range of 100 – 500 nm on 10 July, 2015 and 10 - 100 nm on 11 July, 2015. These are probably also related to the advection phenomenon. However, a contribution of new particle formation cannot be excluded. These aspects need further investigation by exploiting available chemical analyses of aerosol sampled on filters, scanning electron microscopy images and single particle EDX (energy dispersive X-ray) analysis.

Figure 19 shows the temporal trend of some selected aerosol components collected during the BB event in Ny-Ålesund. The plots include a few days before and after the event, in order to highlight differences in atmospheric concentrations. Figures 19a and 19b show the sudden increase of $K^+$ and $SO_4^{2-}$ concentrations for particles with diameter smaller than 10 μm from 10 July onwards. $K^+$, a more specific biomass burning marker (Vassura et al., 2014) increased from about 10 to about 65 ng/m$^3$, with a percentage increase similar to that shown by sulfate. As a comparison, typical sea-spray ($Na^+$) and crustal ($Ca^{2+}$) markers did not show any significant increase during the same period (Figure 19 (c) and (d)). $K^+$ and $SO_4^{2-}$ biomass burning signature is paired with a similar increase of other potential markers such as NH4, $C_2O_4^{2-}$ (oxalate), V, Cd, F, Ni and Pb (not shown here). Crustal components, such as Al, Fe, Ti and Rare Earth Elements (REEs), do not show any particular pattern (not shown here).

In addition, data obtained from the r/v Oceania cruise show some significant increase of the single scattering properties (Figure 20). The first peak of the scattering coefficient was observed between 9 and 10 July and the second between 11 and 12 July (Figure 20a). However, the variability of bc concentration was different and only the second event was observed (Figure 20c). Based on the AE defined for a scattering coefficient at 450 and 700 nm (Figure 20b) the authors conclude that the first episode occurred due to local sea salt production (small AE) while the second was probably due to biomass burning (very high

## 5. Summary and conclusions

In this study the authors described the effects of an intense BB event which took place in Alaska and Canada between late June and early July 2015 and influenced the European Arctic mainly between 9 and 16 July 2015. However, at least 4 weeks later, a shallow aerosol layer still existed in the upper troposphere. In July, unusually high values of AOD were observed over a vast area of the European Arctic from Ny-Ålesund and Hornsund reaching as far as Northern Scandinavia. Ground-based measurements show that the AOD at 500 nm exceeded 1.0 in Ny-Ålesund and 0.8 in Hornsund. Such high values were not observed in Hornsund in the last 10 years and last 15 years in Ny-Ålesund. The previous record of a high air pollution event was observed in Ny-Ålesund in May 2006 (Treffeisen et al., 2007). AOD (500 nm) up to 0.6 (half the value measured in 2015) was related to BB particles being transported from the East European agricultural fires (Stohl et al., 2007). Eck et al., (2009) reported that in another part of the Arctic (Alaska) during the BB events the AOD is much higher and can reach a value of 3 (Bonanza Creek station). In addition, record forest burning extent noted in the years 2004 and 2005 resulted in a monthly average AOD in August of both years that was similar to peak burning season's monthly mean AOD in major BB regions in Brazil and Zambia (Eck et al., 2009).

During the 2015 event relatively high values of AE (about 1.5) indicate the presence of small aerosol particles in the atmosphere, in case of this study, predominantly, smoke particles. Chemical observation at the surface shows a significant increase of the BB concentration markers unlike components such as sea spray and dust markers which were low during the BB event.

The event was simulated by the NAAPS and HYSPLIT models which show the transport of the BB particles emitted in Alaska and Western Canada toward the Arctic Ocean and then towards the south over Spitsbergen and Northern Scandinavia. The NAAPS model estimated the smoke AOD (550 nm) at the value of up to 1 over Alaska and up to 0.8 over the Arctic. We found that the average value of AOD at 550 nm from MODIS was up to 0.7 over the ocean in the south and south west directions over Spitsbergen.

The vertical structure of the BB aerosol plumes obtained from ceilometer and lidar

absorbing aerosols, as can be expected from a flaming combustion of BB particles (Liu et al., 2014; Eck et al., 2009). A very high value of AOD during the BB event can be considered as an extreme with a significant impact on incoming solar radiation. Previous studies of BB events in the Arctic show significant top of the atmosphere (TOA) direct and semi-direct shortwave radiative forcing. For example, the transport of BB from Eastern Europe in the spring of 2008 lead to positive radiative forcing over snow and sea ice with the value of +0.58 W/m$^2$ (Marelle et al., 2015). However, this event was less intensive (lower AOD) in comparison to the 2015 episode.

**Acknowledgements**

The authors would like to acknowledge the support of this research from the Polish-Norwegian Research Programme operated by the National Centre for Research and Development under the Norwegian Financial Mechanism 2009-2014 within the frame of Project Contract No Pol-Nor/196911/38/2013 and also project KNOW, Leading National Research Centre received by the Centre for Polar Studies for the period 2014-2018 established by regulation No. 152 (2013, Nov 14) of the Rector of the University of Silesia.

The authors also acknowledge Brent Holben, Piotr Sobolewski for the use of the data from the AERONET station in Hornsund; Victoria E. Cachorro Revilla, Sandra Blindheim for the data from the Andenes AERONET station and Stergios Vratolis and Kostas Eleftheriadis for providing data from the Zeppelin station.

The authors would also like to thank D. Westphal from the Naval Research Laboratory in Monterey for providing the NAAPS model input (http://www.nrlmry.navy.mil/aerosol/) The NASA Micro-Pulse Lidar Network is funded by the NASA Earth Observing System and the Radiation Sciences Program.

**References**


Alexandrov, M.D., A. Marshak, B. Cairns, A.A. Lacis, and B.E. Carlson, (2004), Automated cloud screening algorithm for MFRSR data. Geophys. Res. Lett., 31, L04118, doi:10.1029/2003GL019105.

Anderson, T. L., Covert, D. S., Marshall, S. F., Laucks, M. L., Charlson, R. J., Waggoner, A. P., Ogren, J. A., Caldow, R., Holm, R. L., Quant, F. R., Sem, G. J., Wiedensohler, A., Ahlquist, N. A., and Bates, T. S., (1996). Performance characteristics of a high-sensitivity, three-wavelength, total scatter/backscatter nephelometer, J. Atmos. Oceanic Technol., 13, 967–986.

Anderson, T. L. and Ogren, J. A., (1998), Determining aerosol radiative properties using the TSI 3563 integrating nephelometer, Aerosol Sci. Tech., 29, 57–69.

Andreae, M. O., and A. Gelencsér, (2006), Black carbon or brown carbon? The nature of light-absorbing carbonaceous aerosols, Atmos. Chem. Phys., 6, 3131-3148, doi:10.5194/acp-6-3131-2006. Bellouin, N., J. Quaas, J.-J. Morcrette, and O. Boucher (2013), Estimates of aerosol radiative forcing from the MACC re-analysis, Atmos. Chem. Phys., 13, 2045-2062, doi:10.5194/acp-13-2045-2013.

Beringer, J., L. B. Hutley, N. J. Tapper, A. Coutts, A. Kerley, and A. P. O'Grady (2003), Fire impacts on surface heat, moisture and carbon fluxes from a tropical savanna in northern Australia, International Journal of Wildland Fire, 12, pp. 333–340.

Bond, T. C., S. Doherty, D. Fahey, P. M. Forster, T. Berntsen, B. J. DeAngelo, M. G. Flanner, S. Ghan, B. Kärcher, D. Koch, S. Kinne, Y. Kondo, P. K. Quinn, M. C. Sarofim, M. G. Schultz, M. Schulz, C. Venkataraman, H. Zhang, S. Zhang, N. Bellouin, S. K. Guttikunda, P. K. Hopke, M. Z. Jacobson, J. W. Kaiser, Z. Klimont, U. Lohmann, J. P. Schwarz, D. Shindell, T. Storelvmo, S. G. Warren, C. S. Zender (2013), Bounding the role of black carbon in the climate system: A scientific assessment, J. Geophys. Res. Atmos., 118, 5380-5552, doi:10.1002/jgrd.50171.

Bovchaliuk, V., A. Bovchaliuk, G. Milinevsky, V. Danylevsky, M. Sosonkin, Ph. Goloub, (2013), Aerosol Microtops II sunphotometer observations over Ukraine, Advances in Astronomy and Space Physics, 3, 46-52.

Brönnimann, S., T. Ewen, J. Luterbacher, R.S. Stolarski, U. Neu, (2008), A focus on climate during the past 100 years. In Climate Variability and Extremes during the Past 100 Years. Springer, pp.1-25, ISBN: 9781402067655, doi: 10.1007/978-1-4020-6766-2_1.

Buonanno, G., Dell'Isola, M., Stabile, L., and Viola, A., (2009), Uncertainty budget of the SMPS-APS system in the measurement of PM10, PM2.5 and PM1, Aerosol Sci. Tech., 43, 1130–1141.

Campbell, J.R., D.L. Hlavka, E.J. Welton, C.J. Flynn, D.D. Turner, J.D. Spinhirne, V.S. Scott, and I.H. Hwang, (2002), Full-time, Eye-Safe Cloud and Aerosol Lidar Observation at Atmospheric Radiation Measurement Program Sites: Instrument and Data Processing", J. Atmos. Oceanic Technol., 19, 431-442.

Chen, W. N., C. W. Chiang, and J. B. Nee (2002), Lidar ratio and depolarization ratio for cirrus clouds, Applied Optics, Vol. 41, Issue 30, 6470-6476.

Chen, Y., J. T. Randerson, D. C. Morton, R. S. DeFries, G. J. Collatz, P. S. Kasibhatla, L. Giglio, Y. Jin, and M. E. Marlier (2011), Forecasting fire season severity in South America using sea surface temperature anomalies, Science, 334, 787–791, doi:10.1126/science.1209472.

Cooke W.F., and J.J.N. Wilson (1996), A global black carbon aerosol model, Journal of Geophysical Research 101: doi: 10.1029/96JD00671. issn: 0148-0227.

Draxler, R.R., and G.D. Hess (1997), Description of the HYSPLIT_4 modeling system. NOAA Tech. Memo. ERL ARL-224, NOAA Air Resources Laboratory, Silver Spring, MD, 24 pp.

Crutzen, P. J., L. E. Heidt, J. P. Krasnec, W. H. Pollock, and W. Seiler (1979), BB as a source of atmospheric gases CO, H2 N2O, NO, CH3Cl and COS, Nature, 282, 253–256.

Dubovik, O. and M.D. King, A (2000), flexible inversion algorithm for the retrieval of aerosol 672 optical properties from Sun and sky radiance measurements, J. Geophys. Res., 105, 673 20673-20696.

Eck, T. F., B. N. Holben, J. S. Reid, O. Dubovik, A. Smirnov, N. T. O'Neill, I. Slutsker, and S. Kinne (1999), Wavelength dependence of the optical depth of biomass burning, urban and desert dust aerosols, J. Geophys. Res., 104, 31,333-31,350.

Geophys. Res. Lett., 36, L02809, doi:10.1029/2008GL035741. Fernandes, K., W. Baethgen, S. Bernardes, R. DeFries, D. G. DeWitt, L. Goddard, W. Lavado, D. E. Lee, C. Padoch, M. Pinedo-Vasquez, and M. Uriarte (2011), North tropical Atlantic influence on western Amazon fire season variability, Geophys. Res. Lett., 38, L12701, doi:10.1029/2011GL047392.

Fernandes, A., Thomas, L., Altaner, C., Callow, P., Forsyth, T., Apperley, D., Kennedy, C., and M. Jarvis (2011), Nanostructure of cellulose microfibrils in spruce wood, PNAS, vol. 108, no. 47, E1195 – E1203.

Field, R. D., G. R. van der Werf, and S. S. P. Shen (2009), Human amplification of drought-induced BB in Indonesia since 1960, Nature Geo., 2, 185–188, doi:10.1038/NGEO443.

Fisher, J. A., D. J. Jacob, M. T. Purdy, M. Kopacz, P. Le Sager, C. Carouge, C. D. Holmes, R. M. Yantosca, R. L. Batchelor, K. Strong, G. S. Diskin, H. E. Fuelberg, J. S. Holloway, E. J. Hyer, W. W. McMillan, J. Warner, D. G. Streets, Q. Zhang, Y. Wang, and S. Wu (2010), Source attribution and interannual variability of Arctic pollution in spring constrained by aircraft (ARCTAS, ARCPAC) and satellite (AIRS) observations of carbon monoxide, Atmos. Chem. Phys., 10, 977–996, doi:10.5194/acp-10-977-2010.

Flentje, H., Heese, B., Reichardt, J., and Thomas, W. (2010), Aerosol profiling using the ceilometer network of the German Meteorological Service, Atmos. Meas. Tech. Discuss., 3, 3643–3673, doi:10.5194/amtd-3-3643-2010.Forster, P., V. Ramawamy, P. Artaxo, T. Berntsen, R. Betts, D.W. Fahey, J. Haywood, J. Lean (2007), Changes in atmospheric constituents and in radiative forcing, Climate Change 2007: the Physical Basis. Contribution of Working Group I to the Fourth Assessment Report of the Intergovernmental Panel on Climate Change, Cambridge University Press, Cambridge, United Kingdom and New York, NY, USA, 129-234.

Frey, S., Poenitz, K., Teschke, G., and Wille, H. (2010), Detection of aerosol layers with ceilometers and the recognition of the mixed layer depth, presented at the International Symposium for the Advancement of Boundary Layer Remote Sensing (ISARS), 2010.

Fromm, M., Shettle, E. P., Fricke, K. H., Ritter, C., Trickl, T., Giehl, H., Gerding, M., Barnes, J., O'Neill, M., Massie, S. T., Blum, U., McDermid, I. S., Leblanc, T., and T.

Graber, E., and Y. Rudich (2006), Atmospheric HULIS: How humic-like are they? A comprehensive and critical review, Atmos. Chem. Phys., 6, 729-753, doi:10.5194/acp-6-729-2006.

Haywood, J.M., and V. Ramaswamy (1998), Global sensitivity studies of the direct radiative forcing due to anthropogenic sulfate and black carbon aerosols, Journal of Geophysical Research 103: doi: 10.1029/97JD03426. issn: 0148-0227.

Heintzenberg, J., Wiedensohler, A., Tuch, T. M., Covert, D. S., Sheridan, P., Ogren, J. A., Gras, J., Nessler, R., Kleefeld, C., Kalivitis, N., Aaltonen, V., Wilhelm, R.-T. and Havlicek, M, (2006), Intercomparisons and Aerosol Calibrations of 12 Commercial Integrating Nephelometers of Three Manufacturers. J. Atmos. Ocean. Tech., 23: 902–914.

Herber, A., L. W. Thomason, H. Gernandt, U. Leiterer, D. Nagel, K.-H. Schulz, J. Kaptur, T. Albrecht, and J. Notholt, (2002), Continuous day and night aerosol optical depth observations in the Arctic between 1991 and 1999, J. Geophys. Res., 107(D10), doi:10.1029/2001JD000536.Hoffmann, A. (2011), Comparative aerosol studies based on multi-wavelength Raman LIDAR at Ny Ålesund, Spitsbergen, PhD Thesis Uni. Potsdam, http://epic.awi.de/29932/1/Hof2011g.pdf.

Hogan, T.F. and T.E. Rosmond (1991), The description of the Navy Operational Global Atmospheric Prediction System's spectral forecast model. Mon. Wea. Rev., 119, 1786-1815.

Holben, B.N., T.F. Eck, I. Slutsker, D. Tanré, J.P. Buis, A. Setzer, E.F. Vermote, J.A. Reagan, Y.J. Kaufman, T. Nakajima, F. Lavenu, I. Jankowiak, and A. Smirnov (1998), AERONET – A federated instrument network and data archive for aerosol characterization, Remote Sensing of Environment, 66, 1: 1-16.

Hyer, E. J., Reid, J. S., and Zhang, J. (2011), An over-land aerosol optical depth data set for data assimilation by filtering, correction, and aggregation of MODIS Collection 5 optical depth retrievals, Atmos. Meas. Tech., 4, 379–408.

IPCC, 2007. Climate Change 2007: The Physical Science Basis. Contribution of Working Group I to the Fourth Assessment Report of the Intergovernmental Panel on Climate Change [Solomon, S., D. Qin, M. Manning, Z. Chen, M. Marquis, K.B. Averyt, M.Tignor

and B.M. Midgley (eds)]. Cambridge University Press, Cambridge, United Kingdom and New York, NY, USA.

Jin, Y. K., K. Kai, T. Kawai, T. Nagai, A. Sakai, A. Yamazaki, D. Uchiyama, N. Batdorj, Sugimoto, and T. Nishizawa (2015), Ceilometer calibration for retrieval of aerosol optical properties, Journal of Quantitative Spectroscopy and Radiative Transfer, 153, 49-56.

Kirchstetter, T.W., T. Novakov, and P.V. Hobbs (2004), Evidence that the spectral dependence of light absorption by aerosols is affected by organic carbon, Journal of Geophysical Research 109: doi: 10.1029/2004JD004999. issn: 0148-0227.

Knobelspiesse, K. D., Pietras, C., Fargion, G. S., Wang, M. H., Frouin, R., Miller, M. A., (2004), Subramaniam, S., and Balch, W. M.: Maritime aerosol optical thickness measured by handheld sunphotometers, Remote Sens. Environ., 93, 87–106.

Kotchenruther, R. A., and P. V. Hobbs (1998), Humidification factors of aerosols from biomass burning in Brazil, J. Geophys. Res., 103(D24), 32081–32089, doi:10.1029/98JD00340.

Lack, D., E. R. Lovejoy , T. Baynard , A. Pettersson, A. R. Ravishankara, (2006), Aerosol Absorption Measurement using Photoacoustic Spectroscopy: Sensitivity, Calibration, and Uncertainty Developments, Aerosol Science and Technology, 40(9), 697-708.

Langenfelds, R. L., R. J. Francey, B. C. Pak, L. P. Steele, J. Lloyd, C. M. Trudinger, and C. E. Allison (2002), Interannual growth rate variations of atmospheric CO2 and its 13C, H2, CH4, and CO between 1992 and 1999 linked to BB, Global Biogeochem. Cy., 16, 1048, doi:10.1029/2001GB001466.

Law, K. S. and A. Stohl, (2007), Arctic air pollution: Origins and impacts, Science, 315(5818), 1537–1540, 2007.

Levy, R. C., Mattoo, S., Munchak, L. A., Remer, L. A., Sayer, A. M., Patadia, F., and Hsu, N. C., (2013), The Collection 6 MODIS aerosol products over land and ocean, Atmos. Meas. Tech., 6, 2989-3034, doi:10.5194/amt-6-2989-2013.

Liousse, C., J.E. Penner, C. Chuang, J.J. Walton, H. Eddleman, H. Cachier (1996), A global three-dimensional model study of carbonaceous aerosols, Journal of Geophysical Research 101: doi: 10.1029/95JD03426. issn: 0148-0227.

Liu, S., Aiken, A. C., Arata, C., Dubey, M. K.; Stockwell, C. E.; Yokelson, R. J.; Stone, E. A.; Jayarathne, T.; Robinson, A.; DeMott, P. J.; Kreidenweis, S. M (2014), Aerosol single scattering albedo dependence on biomass combustion efficiency: Laboratory and field studies, Geophys. Res. Lett., 41, 742–748, doi:10.1002/2013GL058392.

Loveland, T.R. and A.S. Belward, (1997). The IGBP-DIS global 1 km land cover data set, DISCover: First results, International Journal of Remote Sensing 18, 3291–3295.

Lynch, P., Reid, J. S., Westphal, D. L., Zhang, J., Hogan, T. F., Hyer, E. J., Curtis, C. A., Hegg, D. A., Shi, Y., Campbell, J. R., Rubin, J. I., Sessions, W. R., Turk, F. J., & Walker, A. L. (2016). An 11-year global gridded aerosol optical thickness reanalysis (v1.0) for atmospheric and climate sciences. *Geoscientific Model Development, 9*, 1489-1522.

Madonna, F., Amato, F., Vande Hey, J., and Pappalardo, G. (2015), Ceilometer aerosol profiling versus Raman lidar in the frame of the INTERACT campaign of ACTRIS, Atmos. Meas. Tech., 8, 2207-2223, doi:10.5194/amt-8-2207-2015.

Marelle, L., Raut, J.-C., Thomas, J. L., Law, K. S., Quennehen, B., Ancellet, G., Pelon, J., Schwarzenboeck, A., and Fast, J. D., (2015), Transport of anthropogenic and biomass burning aerosols from Europe to the Arctic during spring 2008, Atmos. Chem. Phys., 15, 3831-3850, doi:10.5194/acp-15-3831-2015.

Markowicz, K. M., T. Zielinski, S. Blindheim, M. Gausa, A.K. Jagodnicka, A.E. Kardas, W. Kumala, Sz.P. Malinowski, M. Posyniak, T. Petelski, T. Stacewicz (2012), Study of vertical structure of aerosol optical properties by sun photometers and ceilometer during MACRON campaign in 2007, Acta Geophys., 60(5), 1308-1337, doi: 10.2478/s11600-011-0056-7.

Markowicz, K.M., M.T. Chilinski, J. Lisok, O. Zawadzka, I.S. Stachlewska, L. Janicka, A. Rozwadowska, P. Makuch, P. Pakszys, T. Zielinski, T. Petelski, M. Posyniak, A. Pietruczuk, A. Szkop, D.L. Westphal, (2016), Study of aerosol optical properties during long-range transport of biomass burning from Canada to Central Europe in July 2013, Journal of Aerosol Scence, 101, 156–173.

Marlon, J. R., P. J. Bartlein, C. Carcaillet, D. G. Gavin, S. P. Harrison, P. E. Higuera, F. Joos, M. J. Power, and I. C. Prentice (2008), Climate and human influences on global BB over

Maturilli, M., Herber, A., and König-Langlo, G., (2015), Surface radiation climatology for Ny-Ålesund, Svalbard (78.9°N), basic 30 observations for trend detection, Theor. Appl. Climatol., 120, 331-339, doi: 10.1007/s00704-014-1173-4.

Morganti, A., Becagli, S., Castellano, E., Severi, M., Traversi, R., Udisti, R., (2007), An improved flow analysis–ion chromatography method for determination of cationic and anionic species at trace levels in Antarctic ice cores. Anal. Chim. Acta 603, 190–198.

Morys, M., F. M. III. Mims, S. Hagerup (2001), Design, calibration, and performance of MICROTOPS II handheld ozone monitor and Sun photometer, J. Geophys. Res.: Atmospheres, 106, 14573.

Müller, T., A. Nowak, A. Wiedensohler, P. Sheridan, M. Laborde, David S. Covert, Angela Marinoni, Kornélia Imre, Bas Henzing, Jean-Claude Roger, Sebastiao Martins dos Santos, Reinhard Wilhelm, Ya-Qiang Wang & Gerrit de Leeuw, (2009), Angular Illumination and Truncation of Three Different Integrating Nephelometers: Implications for Empirical, Size-Based Corrections. Aerosol Science and Technology 43:6, 581-586.

Mtetwa, L., and M.P. McCormick (2003), Development of BB Gaseous and Particulate Emissions Database for Assimilation Into Air Quality Forecast Systems., AGU Fall Meeting Abstracts, 2003, B1062.

Myhre, G., B. H. Samset, M. Schulz, Y. Balkanski, S. Bauer, T. K. Berntsen, H. Bian, N. Bellouin, M. Chin, T. Diehl, R. C. Easter, J. Feichter, S. J. Ghan, D. Hauglustaine, T. Iversen, S. Kinne, A. Kirkevåg, J.-F. Lamarque, G. Lin, X. Liu, M. T. Lund, G. Luo, X. Ma, T. van Noije, J. E. Penner, P. J. Rasch, A. Ruiz, Ø. Seland, R. B. Skeie, P. Stier, T. Takemura, K. Tsigaridis, P. Wang, Z. Wang, L. Xu, H. Yu, F. Yu, J.-H. Yoon, K. Zhang, H. Zhang, and C. Zhou (2013), Radiative forcing of the direct aerosol effect from AeroCom Phase II simulations, Atmos. Chem. Phys., 13, 1853-1877, doi:10.5194/acp-13-1853-2013.

Natural Resources Canada, Canadian Wildland Fire Information System (Atmospheric Dispersion Index), http://cwfis.cfs.nrcan.gc.ca/maps/wx?type=adi&year=2015&month=6&day=23 (accessed 21.04.2016).

aerosol optical depth and Ångström exponent over Spitsbergen, Springer Series: GeoPlanet: Earth and Planetary Sciences; ISBN 978-3-319-14282-1, pp. 23-37.

Pietruczuk, A. and G. Karasinski (2010), LIDAR at Polish Polar Station, instrument design and first results, Proc. 25th International Laser Radar Conference, 5–9 July 2010, St. Petersburg, Russia, 163–165.

Power, M. J., J. Marlon, N. Ortiz, P. J. Bartlein, S. P. Harrison, F. E. Mayle, A. Ballouche, R. H. W. Bradshaw, C. Carcaillet, and C. Cordova (2008), Changes in fire regimes since the Last Glacial Maximum: an assessment based on a global synthesis and analysis of charcoal data, Clim. Dyn., 30, 887–907, doi:10.1007/s00382-007-0334-x.

Ramanathan, V., P. J. Crutzen, J. T. Kiehl, and D. Rosenfeld, (2001), Aerosols, climate, and the hydrological cycle. Science, 294, 2119-2124.

Reid, J. S., Koppmann, R., Eck, T. F., and Eleuterio, D. P., (2005), A review of biomass burning emissions part II: intensive physical properties of biomass burning particles, Atmos. Chem. Phys., 5, 799-825, doi:10.5194/acp-5-799-2005.

Reid, J. S., Hyer, E. J., Prins, E. M., Westphal, D. L., Jianglong, Z., Jun, W., Christopher, S. A., Curtis, C. A., Schmidt, C. C., Eleuterio, D. P., Richardson, K. A., and Hoffman, J. P.: Global Monitoring and Forecasting of Biomass-Burning Smok, (2009), Description of and Lessons From the Fire Locating and Modeling of Burning Emissions (FLAMBE) Program, Selected Topics in Applied Earth Observations and Remote Sensing, IEEE Journal of Selected Topics in Applied Earth Observations and Remote Sensing, 2, 144–162.

Ritter, C., R. Neuber, A. Schulz, K.M. Markowicz, I.S. Stachlewska, J. Lisok, P. Makuch , P. Pakszys, P. Markuszewski, A. Rozwadowska, T. Petelski, T. Zielinski, S. Becagli, R. Traversi, R. Udisti, M. Gausa (2016), 2014 iAREA campaign on aerosol in Spitsbergen - Part 2: optical properties from Raman-lidar and in-situ observations at Ny-Ålesund, *Atmospheric Environment* 141, 1-19.

Sahu, L. K., V. Sheel, K. Pandey, R. Yadav, P. Saxena and S. Gunthe, (2015), Regional biomass burning trends in India: Analysis of satellite fire data, J. Earth Syst. Sci. 124, pp. 1377–1387.

analysis of in-situ spectral aerosol optical properties by a multi-instrumental approach, Atmos. Meas. Tech., 7, 2373-2387, doi:10.5194/amt-7-2373-2014.

Shi, Y., Zhang, J., Reid, J. S., Liu, B., and Hyer, E. J.(2014), Critical evaluation of cloud contamination in the MISR aerosol products using MODIS cloud mask products, Atmos. Meas. Tech., 7, 1791-1801.

Smirnov, A., Holben, B.N., Eck, T.F., Dubovik, O., (2000), Cloud-Screening and quality control algorithms for the AERONET database. Remote Sens. Environ. 73, 337e349.

Spessa, A., B. McBeth, and C. Prentice (2005), Relationships among fire frequency, rainfall and vegetation patterns in the wet-dry tropics of northern Australia: an analysis based on NOAAAVHRR data, Global Ecology and Biogeography, 14, 439–454, doi:10.1111/j.1466-822x.2005.00174.x.

Spinhirne, J.D., J.A.R. Rall, and V.S. Scott (1995), Compact Eye Safe Lidar Systems, Rev. Laser Eng., 23, 112-118.

Stock, M. (2010), Characterization of tropospheric aerosol variability in the European Arctic, PhD Thesis Uni. Potsdam 2010, http://opus.kobv.de/ubp/volltexte/2010/4920/.

Stohl, A. (2006), Characteristics of atmospheric transport into the Arctic troposphere, J. Geophys. Res.-Atmos., 111, D11306,doi:10.1029/2005jd006888.

Stohl, A., Berg, T., Burkhart, J. F., Fjæraa, A. M., Forster, C., Herber, A., Hov, Ø., Lunder, C., McMillan, W. W., Oltmans, S., Shiobara, M., Simpson, D., Solberg, S., Stebel, K., Ström, J., Tørseth, K., Treffeisen, R., Virkkunen, K., and Yttri, K. E., (2007), Arctic smoke – record high air pollution levels in the European Arctic due to agricultural fires in Eastern Europe in spring 2006, Atmos. Chem. Phys., 7, 511-534, doi:10.5194/acp-7-511-2007.

Tomasi, C.; Lupi, A.; Mazzola, M.; Stone, R.S.; Dutton, E.G.; Herber, A.; Radionov, V.F.; Holben, B.N.; Sorokin, M.G.; Sakerin, S.M.; Terpugova, S.A.;Sobolewski, P.S.; Lanconelli, C.; Petkov, B.H.; Busetto, M.; Vitale, V., (2012), An update on Polar aerosol optical properties using POLAR-AOD and other measurements performed during the International Polar Year, Atmos. Environ 52, 29–47.

Toledano, C., Cachorro, V., Gausa, M., Stebel, K., Aaltonen, V., Berjon, A., Ortiz, J. P.,

Tosca, M., J. Randerson, and C. Zender (2013), Global impact of smoke aerosols from landscape fires on climate and the Hadley circulation, Atmos. Chem. Phys., 13, 5227–5241, 2013, doi:10.5194/acp-13-5227-2013.

Torres, O., P. Bhartia, J. Herman, and Z. Ahmad (1998), Derivation of aerosol properties from satellite measurements of backscattered ultraviolet radiation: Theoretical basis, J. Geophys. Res. 103, 17,099–17,110.

Torres, O., A. Tanskanen, B. Veihelmann, C. Ahn, R. Braak, P. Bhartia, P. Veefkind, P. Levelt (2007), Aerosols and surface UV products from Ozone Monitoring Instrument observations: An overview, 112, D24S47, doi:10.1029/2007JD008809.

Treffeisen, R., Tunved, P., Ström, J., Herber, A., Bareiss, J., Helbig, A., Stone, R. S., Hoyningen-Huene, W., Krejci, R., Stohl, A., and Neuber, R., (2007), Arctic smoke – aerosol characteristics during a record smoke event in the European Arctic and its radiative impact, Atmos. Chem. Phys., 7, 3035-3053, doi:10.5194/acp-7-3035-2007.

Turetsky, M. R., E. S. Kane, J. W. Harden, R. D. Ottmar, and K. L. Manies (2011), Recent acceleration of BB and carbon losses in Alaskan forests and peatlands, Nature Geosci., 4, 27–31.

van der Werf, G. R., Randerson, J. T., Giglio, L., Collatz, G. J., Mu, M., Kasibhatla, P. S., Morton, D. C., DeFries, R. S., Jin, Y., and van Leeuwen, T. T., (2010), Global fire emissions and the contribution of deforestation, savanna, forest, agricultural, and peat fires (1997–2009), Atmos. Chem. Phys., 10, 11707-11735, doi:10.5194/acp-10-11707-2010.

Vassura, I., Venturini, E., Marchetti, S., Piazzalunga, A., Bernardi, E., Fermo, P., Passarini, F., (2014), Markers and influence of open biomass burning on atmospheric particulate size and composition during a major bonfire event, Atmos. Environ., 82 , 633 21-225.

Wang, S.-H., N.-H. Lin, M.-D. Chou, and J.-H. Woo (2007), Estimate of radiative forcing of Asian biomass-burning aerosols during the period of TRACE-P, J. Geophys. Res., 112, D10222, doi:10.1029/2006JD007564.

Ward, D. S., S. Kloster, N. M. Mahowald, B. M. Rogers, J. T. Randerson, and P. G. Hess (2012), The changing radiative forcing of fires: global model estimates for past, present and future, Atmos. Chem. Phys., 12, 10857–10886, doi:10.5194/acp-12-10857-2012.

Westerling, A. L., H. G. Hidalgo, D. R. Cayan, and T. W. Swetnam (2006), Warming and earlier spring increase western U.S. forest wildfire activity, Science, 313, 940–943, doi:10.1126/science.1128834.

Witek, M.L., P.J. Flatau, P.K. Quinn, and D.L. Westphal (2007), Global sea-salt modeling: Results and validation against multicampaign shipboard measurements, J. Geophys. Res.112, D08215, DOI: 10.1029/2006JD007779.

Zawadzka, O., K. M. Markowicz, A. Pietruczuk, T. Zielinski, J. Jarosławski, (2013), Impact of urban pollution emitted in Warsaw on aerosol properties, Atmospheric Environment 69, 15–28.

Zhang, J. and Reid, J. S. (2006), MODIS Aerosol Product Analysis for Data Assimilation: Assessment of Level 2 Aerosol Optical Thickness Retrievals, J. Geophys. Res.-Atmos., 111, 22207, doi:10.1029/2005JD006898.

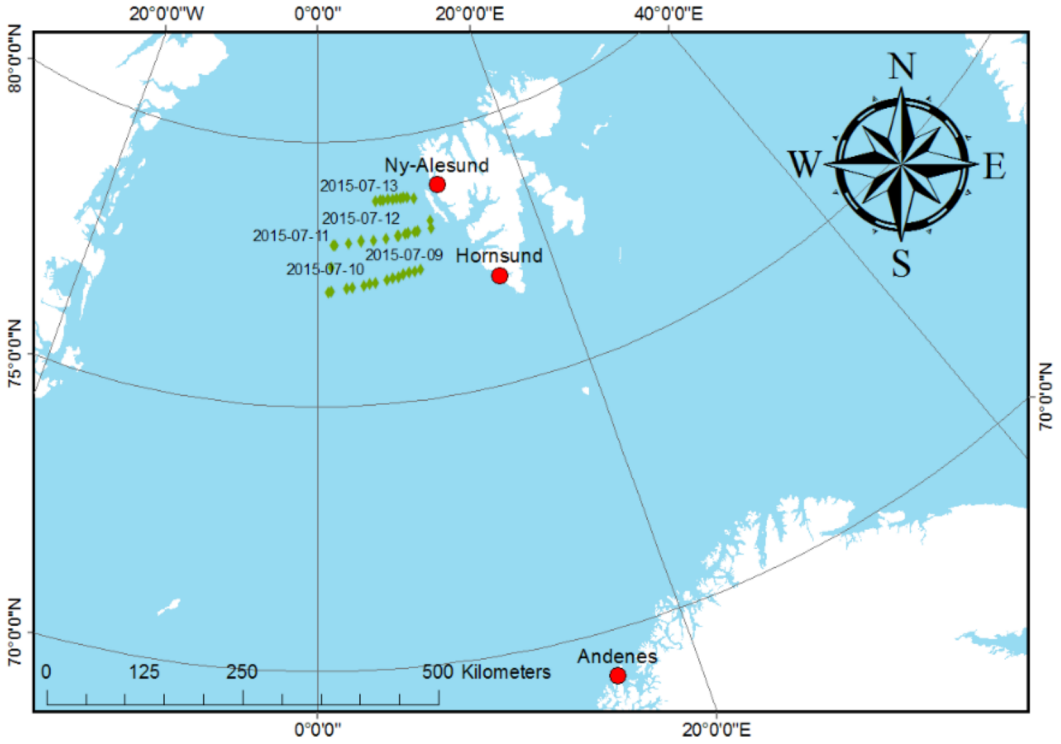


Figure 1. Location of the measurement stations described in the paper (red dots) and the position of the r/v Oceania (green diamonds) between 9 and 13 July of 2015.

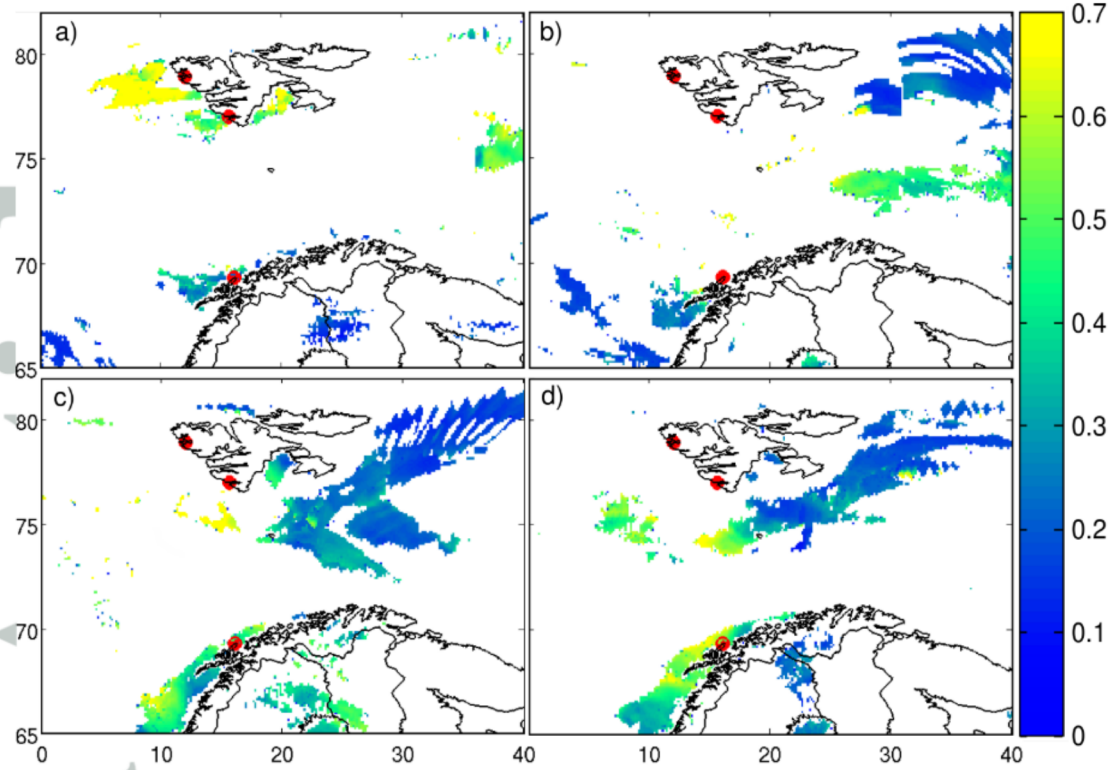


Figure 2. MODIS obtained daily means of AOD at 550 nm for (a) 10, (b) 11, (c) 12, and (d) 13 July 2015. Red dots correspond to Ny-Ålesund, Hornsund, and Andenes.

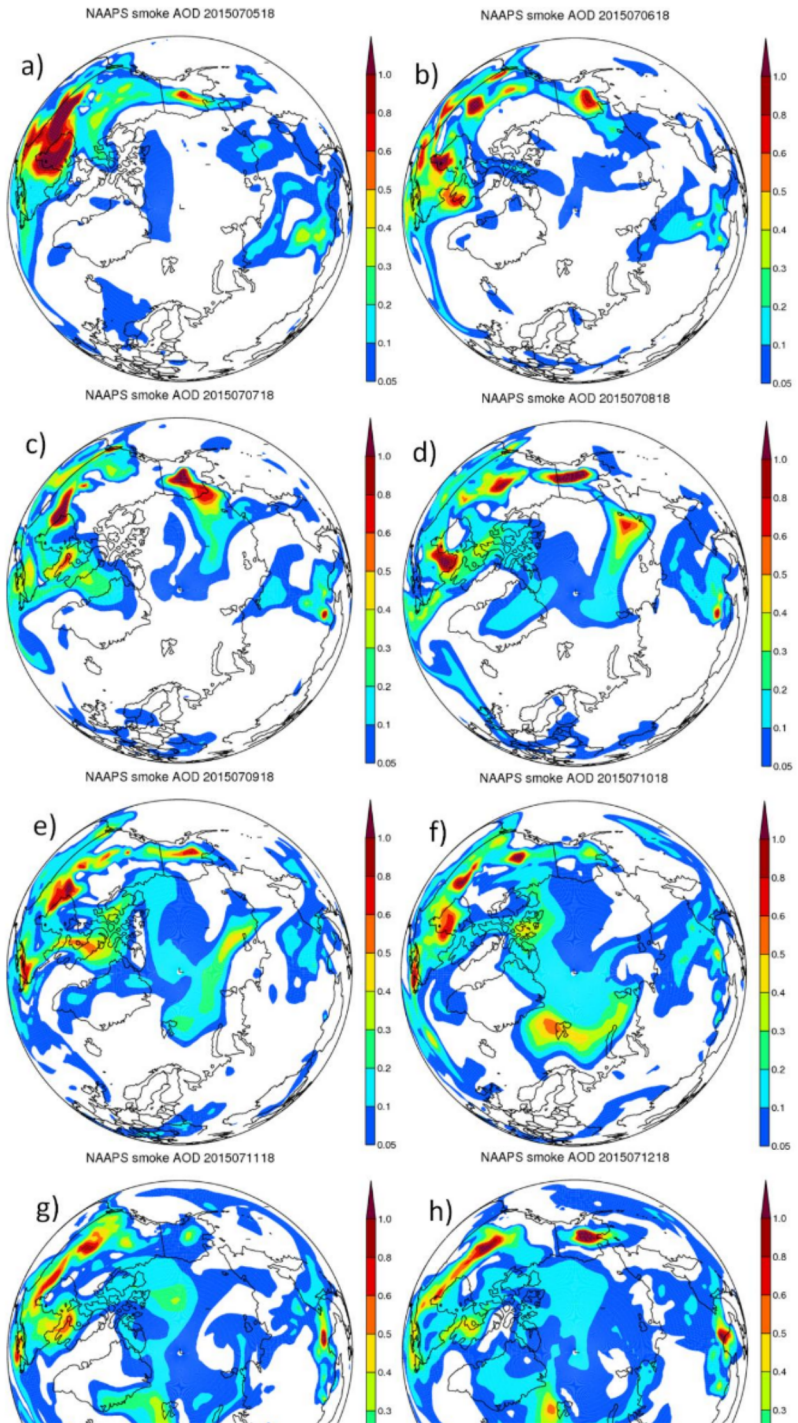

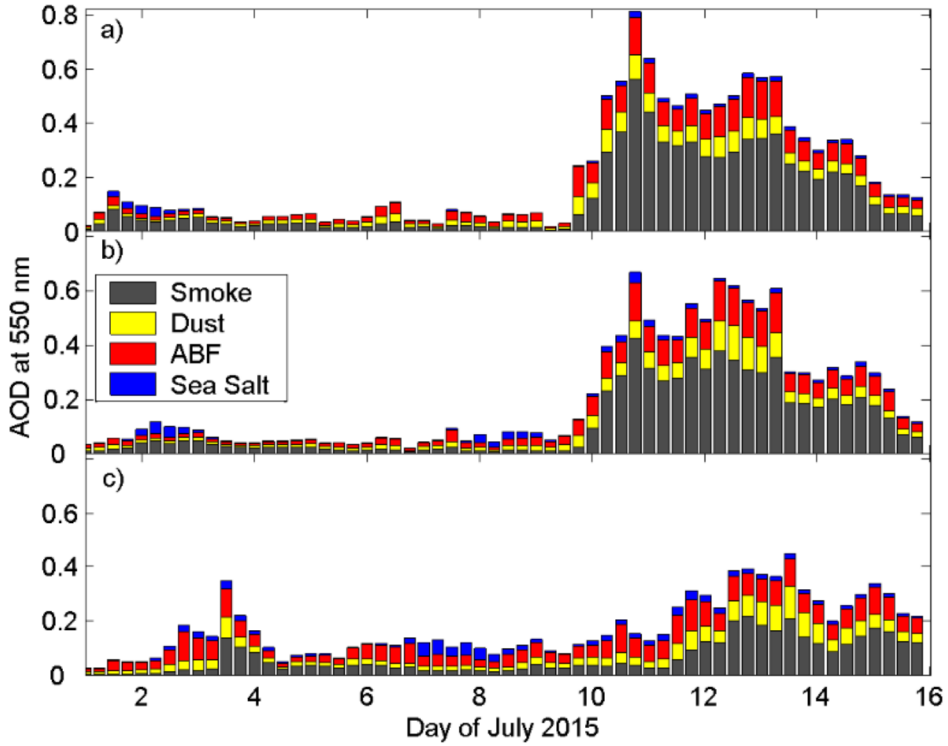


Figure 4. Temporal variability of NAAPS AOD at 550 nm for (a) Ny-Ålesund, (b) Hornsund, and (c) Andenes between 1 and 16 July 2016. Grey, yellow, red and blue bars correspond to smoke, dust, anthropogenic and biogenic fine (ABF), and sea salt particles, respectively.

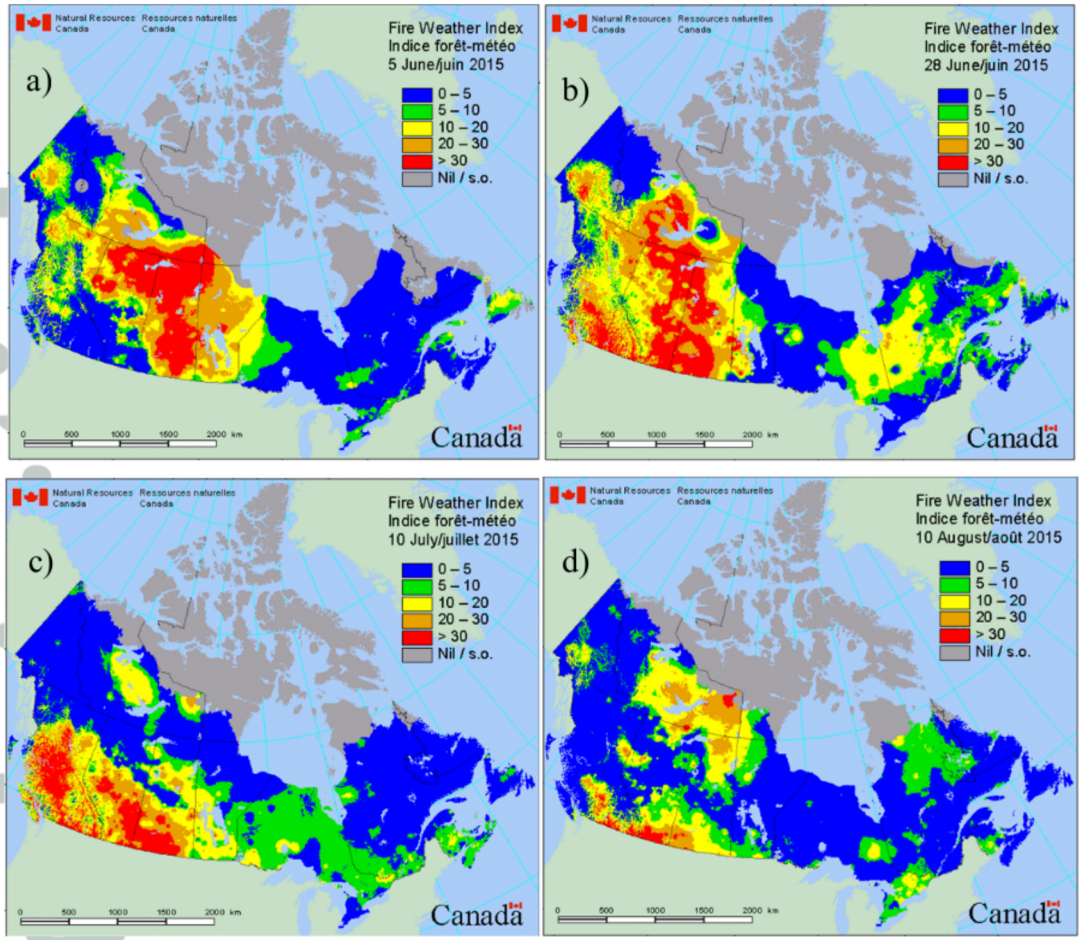


Figure 5. Daily fire M3 (Fire Monitoring, Mapping, and Modeling System) hotspots provided by the Canadian Wildland Fire Information System based on the AVHRR, MODIS and VIIRS satellite observations for (a) 5 June, (b) 28 June, (c) 10 July, and (d) 10 August 2015.

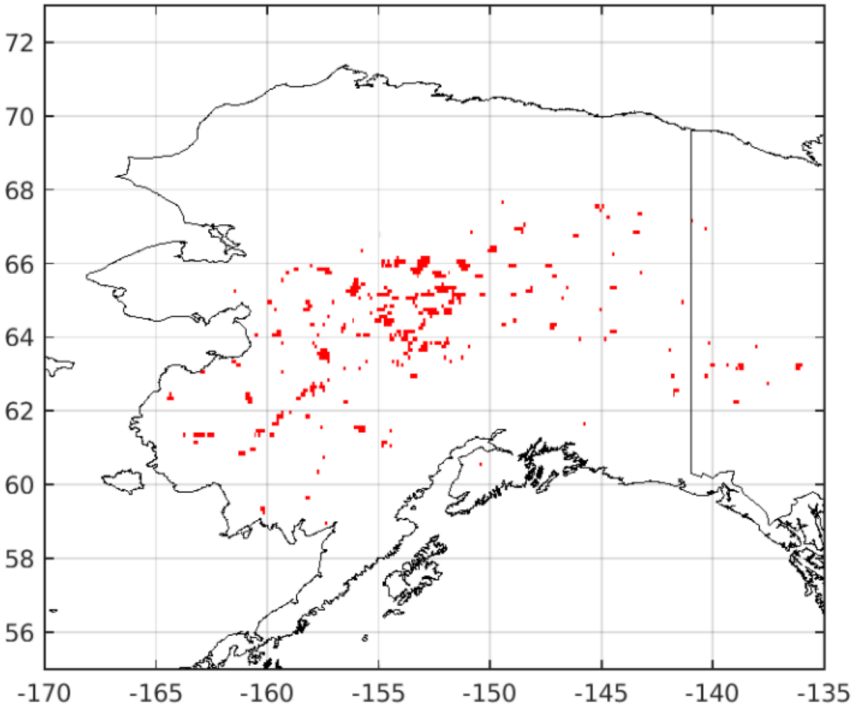


Figure 6. Location of individual fire spots (probability>70%) existing between 19 June – 10 July 2015 in Alaska, gridded to 0.1x0.1º resolution obtained from MODIS data (MCD14ML product, collection 5.1).

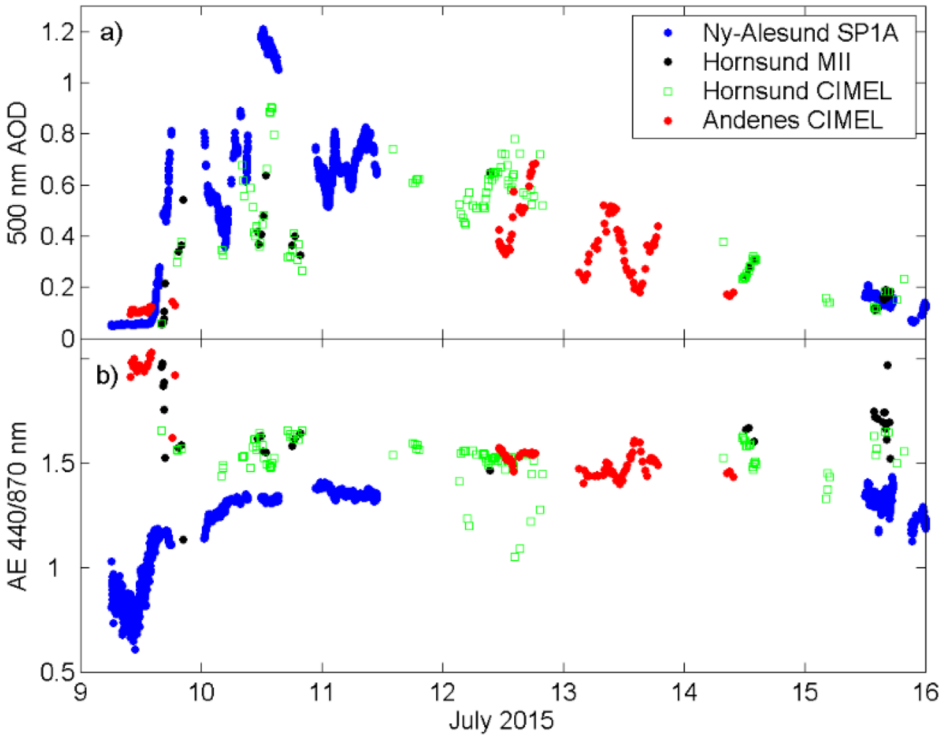


Figure 7. Temporal variability of (a) AOD (at 500 nm) and (b) AE (440/870 nm) measured with sunphotometers between 9 and 16 July 2015. Black dots and blue square markers correspond to Hornsund results obtained from Microtops II and CIMEL, blue dots to Ny-Ålesund (SP1A), and red dots to Andenes (CIMEL).

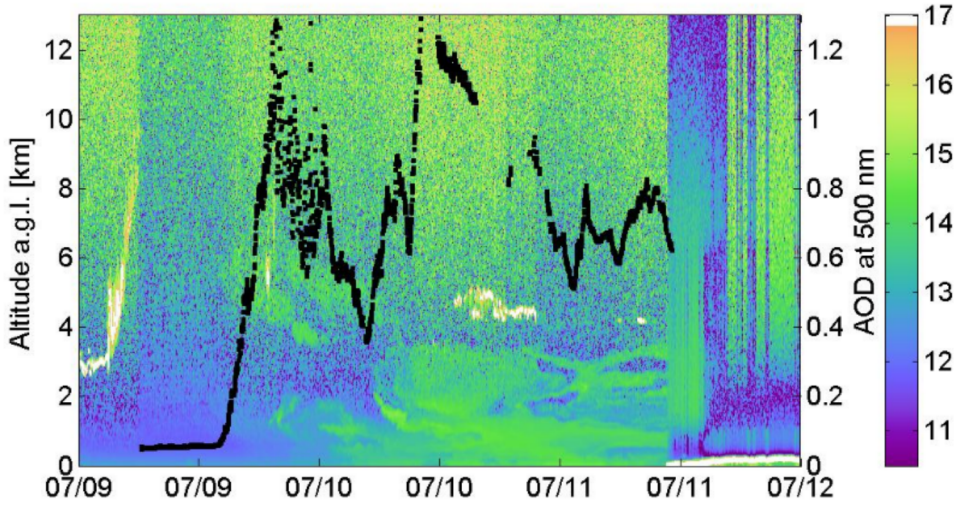


Figure 8. A logarithm of CL51 range corrected signal and SP1A AOD (500 nm) (black dots) over Ny-Ålesund between 9 and 12 July 2015.

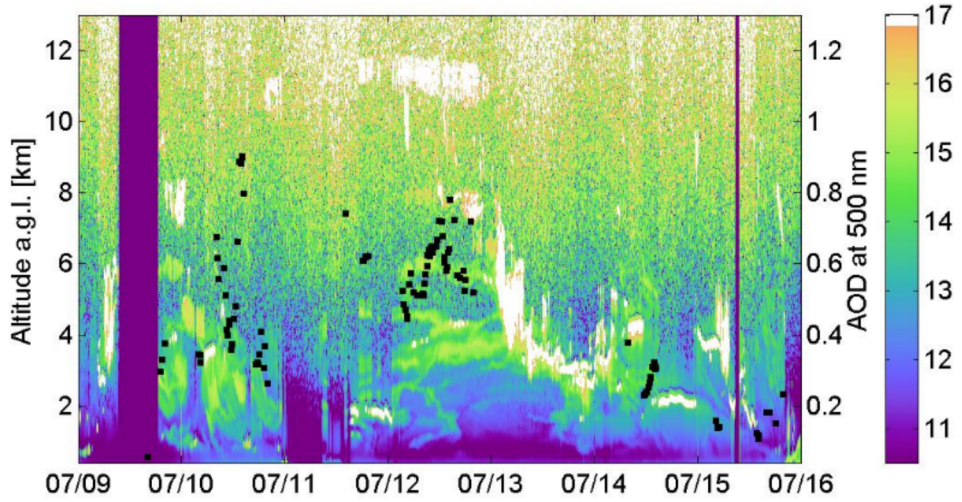


Figure 9. A logarithm of the CHM15K range corrected signal in arbitrary units together with the AERONET based AOD (500 nm; level 2.0) (black dots) over Hornsund between 9 and 16 July 2015.

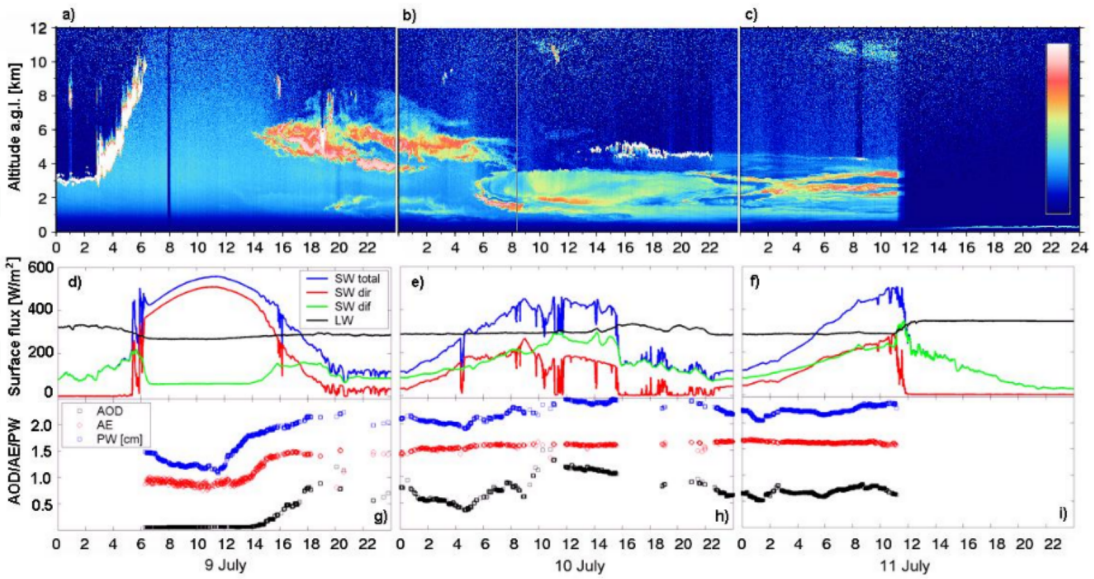


Figure 10. (a-c) the range corrected signal at 523 nm in arbitrary units from the micro-pulse lidar (MPL), (d-f) diurnal cycle of incoming surface shortwave total (blue line), direct (green line), and diffuse (red line)and longwave (black line) radiation flux in W/m$^2$ from CMP22 pyranometers, CHP1 pyrheliometer, and PIR pyrgeometer, and (g-i) the temporal variability of AOD at 500 nm (black squares), AE (red circles), as well as the total precipitable water (blue squares) in cm from SP1A sunphotometer measured over Ny-Ålesund. Panels (a, d, g) correspond to observations performed on 9 July, panels (b, e, h) to 10 July and panels (c, f, i) to 11 July 2015. In case of the MPL data, the white color shows cloud layers, the red color cloud or aerosol layers, while yellow, green and blue show aerosol layers.

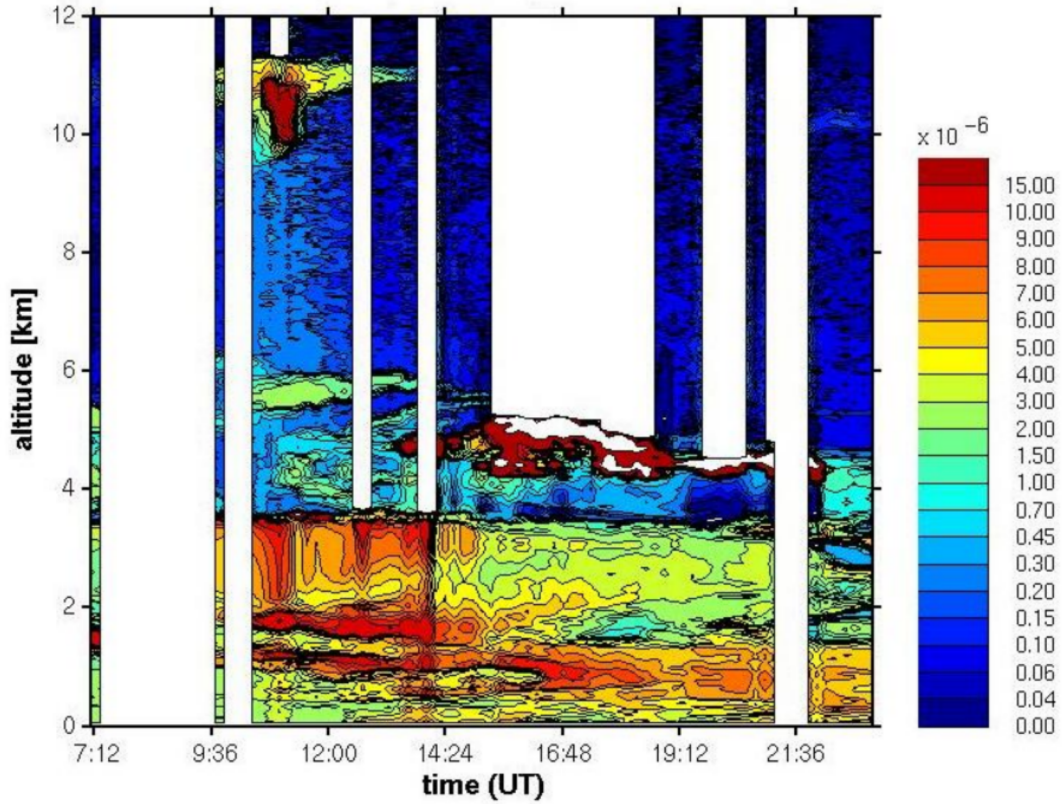


Figure 11. Vertical profiles of backscattering coefficient [$m^{-1} \cdot sr^{-1}$] at 532 nm from the KARL lidar on 10 July 2015 over Ny-Ålesund. White stripes represent multiple scattering above the optically dense layer or breaks in lidar observations.

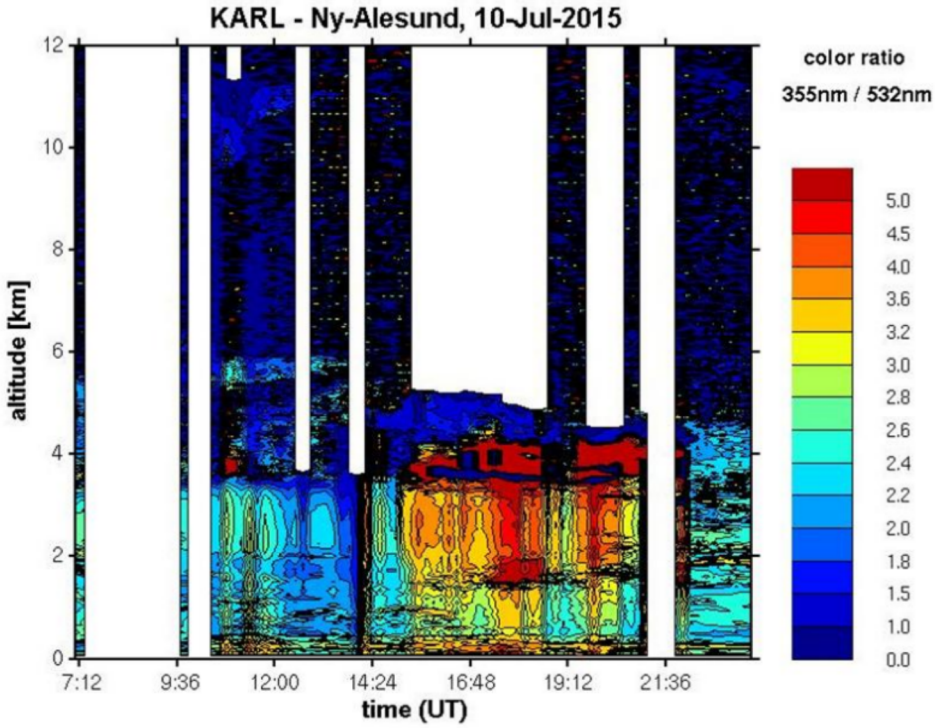


Figure 12. Vertical profiles of the color ratio (355 nm / 532 nm from the KARL lidar on 10 July 2015 over Ny-Ålesund. White stripes represent multiple scattering above the optically dense layer or breaks in lidar observations.

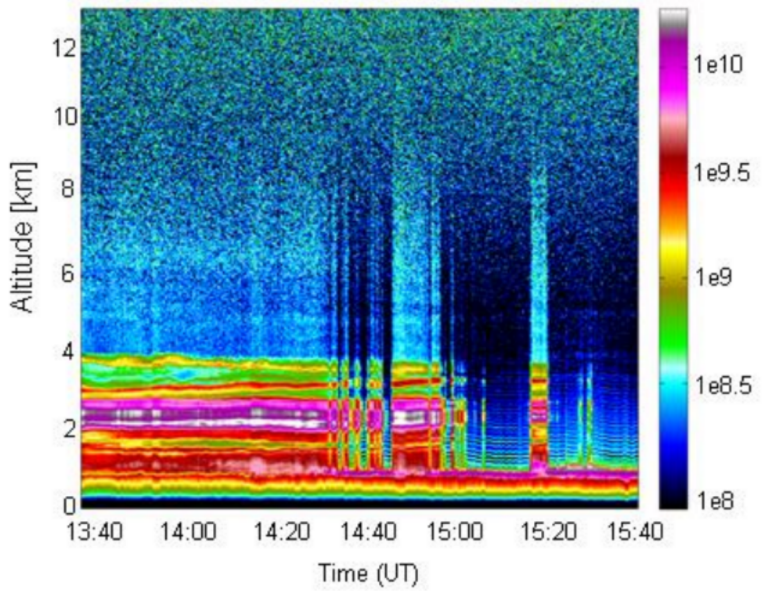


Figure 13. A logarithm of the range corrected signal at 1064 nm in arbitrary units from a lidar deployed at the Polish Polar Station in Hornsund on 10 July 2015.

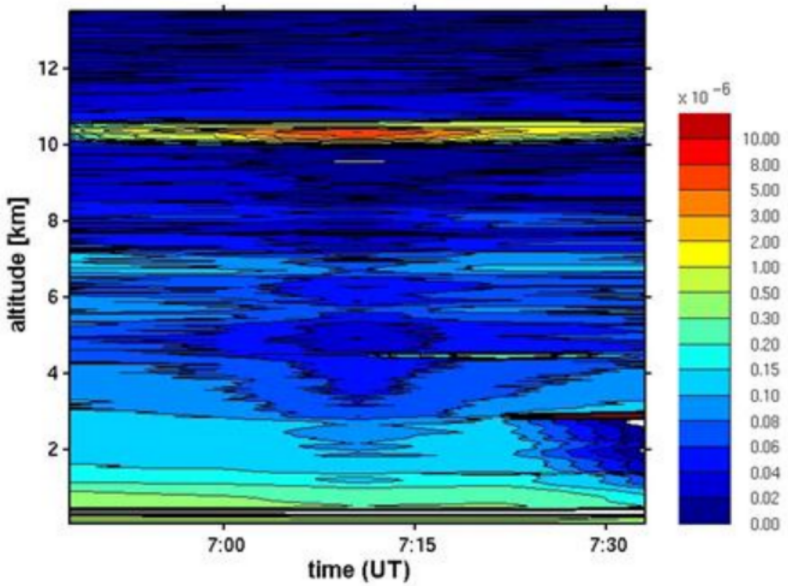


Figure 14. Vertical profiles of the backscattering coefficient [$m^{-1} \cdot sr^{-1}$] at 532 nm from the AWI KARL lidar on 11 August 2015 over Ny-Ålesund.

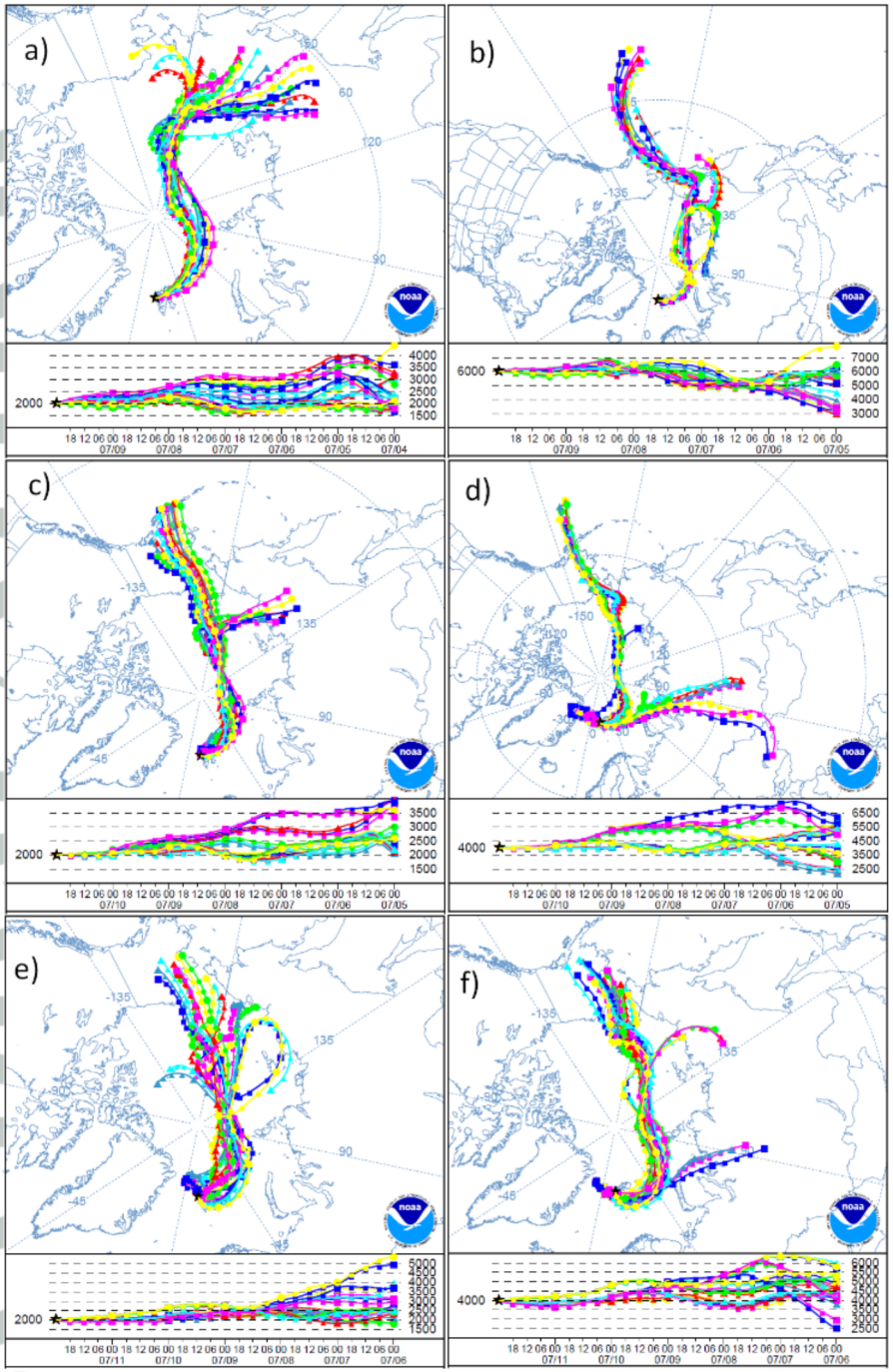

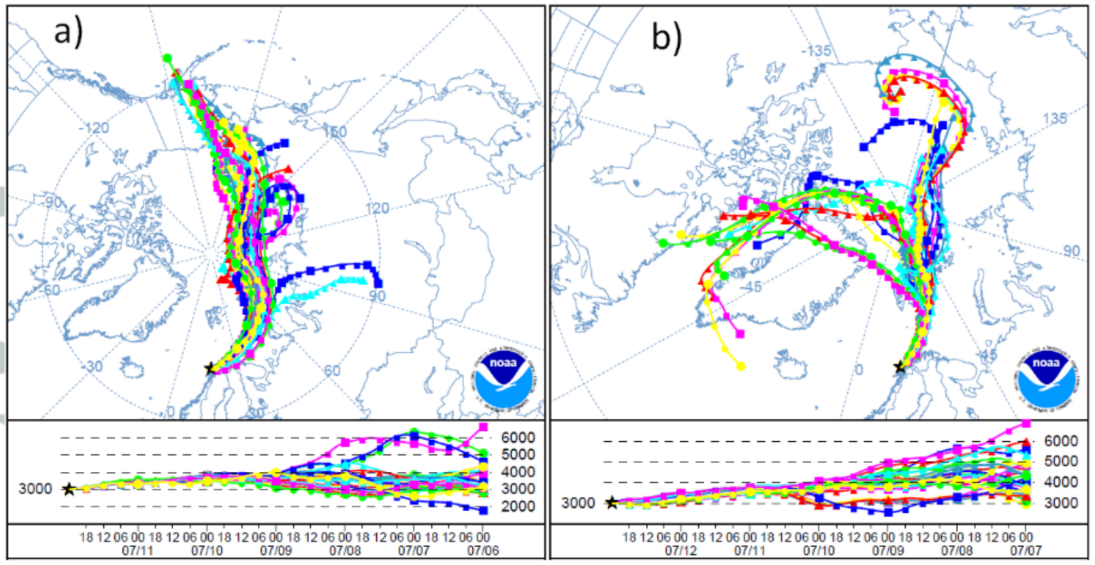


Figure 16. 144-hour air mass ensemble of back trajectories obtained from the NOAA HYSPLIT model at 00:00 UTC for (a) 12 and (b) 13 July 2015 for Andenes. Panels are generated by means of the NCEP/NCAR meteorological database for Ny-Ålesund at 3 km a.s.l.

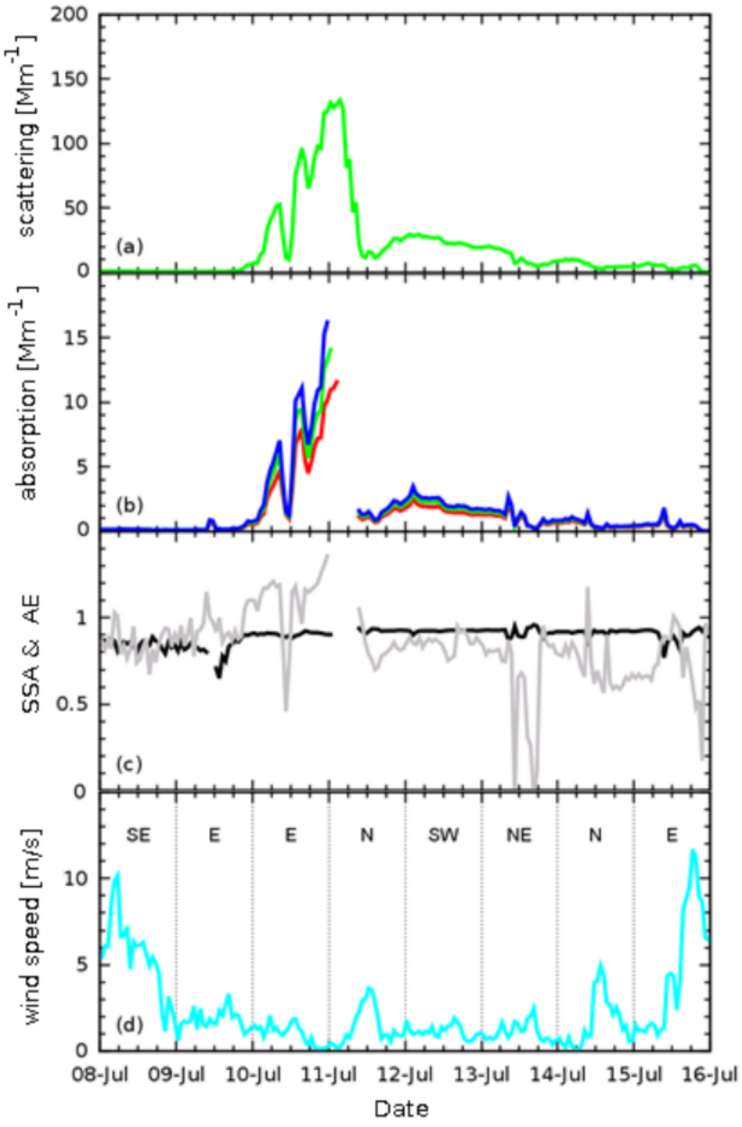


Figure 17. An hourly average of (a) aerosol scattering at 530 nm, and (b) absorption coefficients at 467 (blue), 530 (green), 660 nm (red) in $Mm^{-1}$ plotted with (c) single scattering albedo at 530 nm (gray line) and absorbing AE (black line) measured at the Gruvebadet station (Ny-Ålesund) and (d) wind speed in m/s and direction.

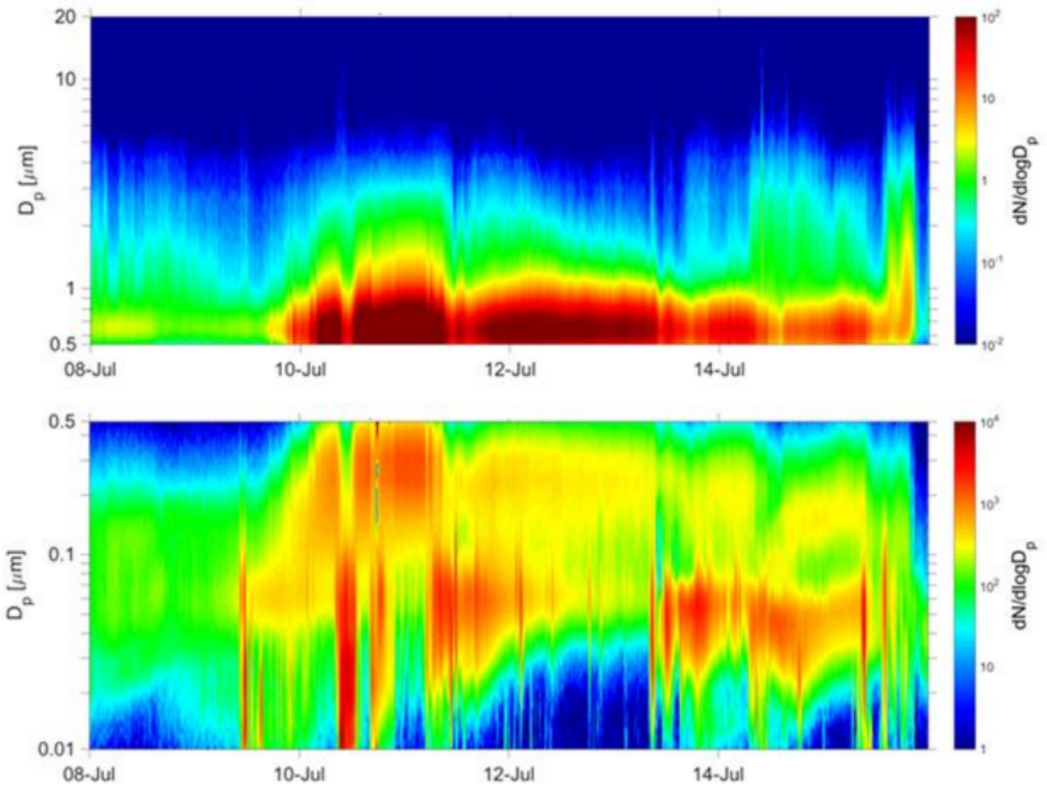


Figure 18. Averaged size distribution and average particle concentration obtained from the APS (upper panel) and SMPS (bottom panel) data for 8-15 July 2015 at the Gruvebadet station (Ny-Ålesund).

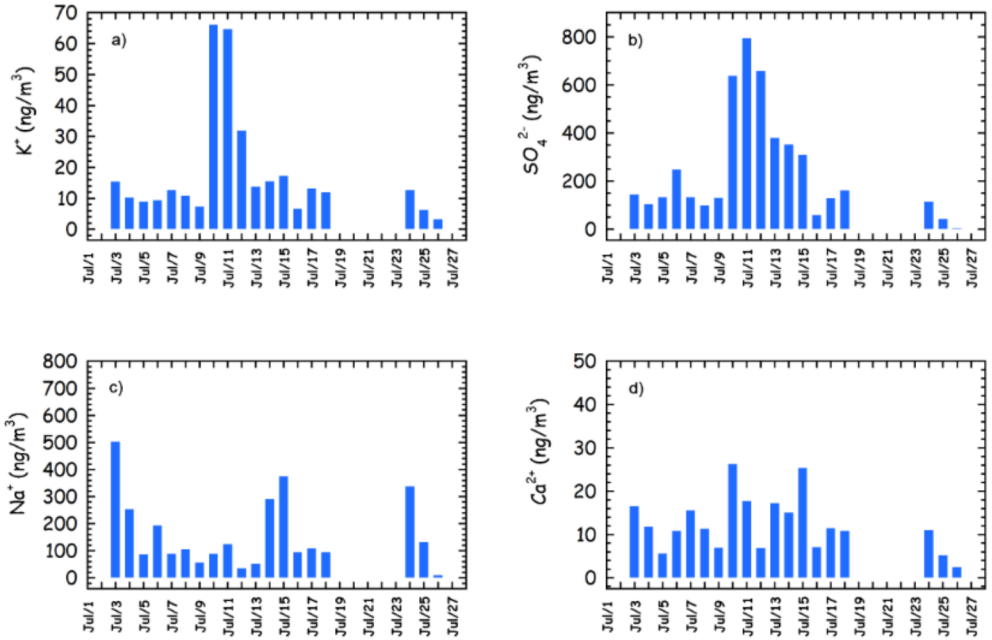


Figure 19. Daily mean concentration of (a) $K^+$, (b) $SO_4^{-2}$, (c) $Na^+$, and (d) $Ca^{2-}$ of PM10 between 1 and 27 July 2015 measured at the Gruvebadet station (Ny-Ålesund).

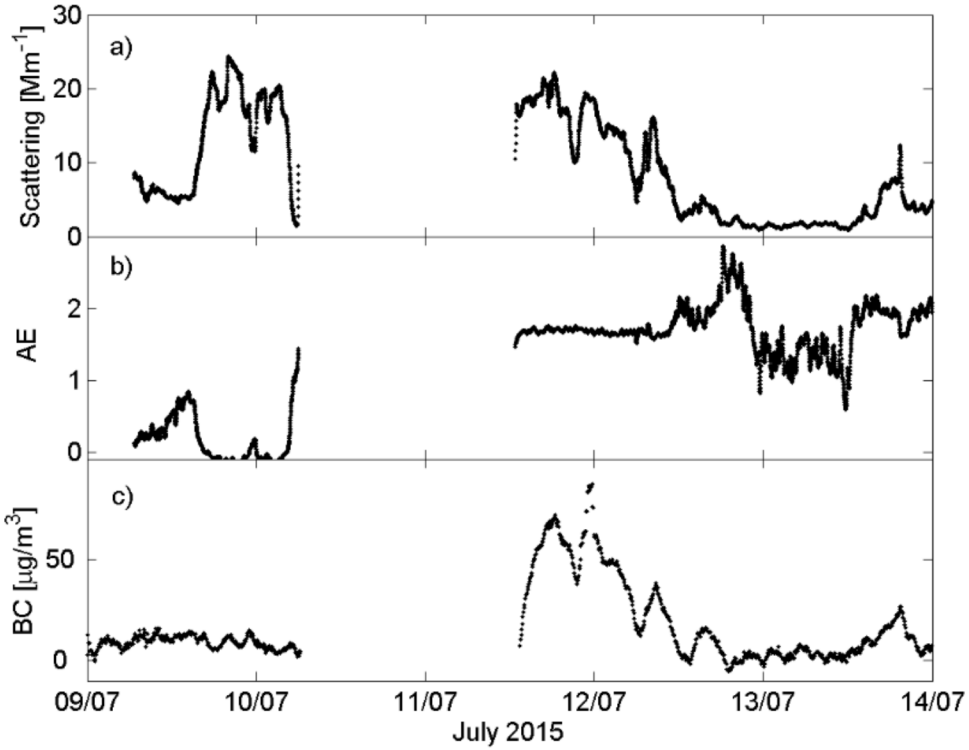


Figure 20. (a) Temporal variability of aerosol scattering coefficient at 550 nm in Mm$^{-1}$, (b) Angstrom Exponent defined for the scattering coefficient at 450 and 700 nm and (c) BC concentration shown in µg/m$^3$, measured between 9 and 13 July 2015 onboard the r/v Oceania.

Table 1. Instruments used for studies of aerosol optical properties during the iAREA campaign in summer 2015. Δt corresponds to the time resolution of the measurements.

| **Ground based Instrument** | **Acronym** | **Wavelength [nm]; Range, Size [nm]** | **Quantities** | **Δt** | **Station** |
|---|---|---|---|---|---|
| AWI Aerosol Raman Lidar KARL | KARL | 355, 387, 532, 607, 1064 | Extinction coefficient Backscatter coefficient Depolarization included | 1 min | Ny-Ålesund |
| AWI Sun photometer SP1A | SP1A | 369, 381, 413, 500, 610, 674, 779, 860, 945, 1023 | AOD, AE, PW | 1 min | Ny-Ålesund |
| Micro-pulse lidar | MPL | 523 | Extinction coefficient Backscatter coefficient | 5 min | Ny-Ålesund |
| AE-31 Aethalometer | AE-31 | 370, 470, 520, 590, 660, 880, 950 | BC | 5 min | Ny-Ålesund (Zeppelin) Oceania |
| Scanning Mobility Particle Sizer Spectrometer SMPS 3034 | SMPS | 10-487 | Size distribution Particle concentration | 10 min | Ny-Ålesund (Gruvebadet observatory) |
| Aerodynamic Particle Sizer APS 3321 | APS | 523-20 000 | Size distribution Particle concentration | 10 min | Ny-Ålesund (Gruvebadet observatory) |
| Particle Soot Absorption Photometer | PSAP | 467, 530, 660 | Absorption coefficient | 1 min | Ny-Ålesund (Gruvebadet observatory) |
| Nephelometer M903 | NEPH | 530 | Scattering coefficient | 10 sec | Ny-Ålesund (Gruvebadet observatory) |
| Nephelometer 3563 | NEPH | 450, 550, 700 | Scattering coefficient, AE | 1 min | Oceania |

| | | | | | |
|---|---|---|---|---|---|
| Microtops II Sun Photometer | MII | 440, 500, 675, 870, 1020 | AOD, AE | Periodic | Hornsund Ny-Ålesund |
| Sunphotometer CIMEL | CIMEL | 340, 380, 440, 500, 675, 870, 939, 1020 | AOD, AE, PW | Periodic | Hornsund Andenes |
| Lidar at Polish Polar Station Hornsund | Raman lidar | 355, 532,1064, 387, 407 | Extinction coefficient Backscatter coefficient | 0.3 min | Hornsund |
| Pyrheliometer | CHP1 | 280-4000 | Direct Solar flux | 1 min | Ny-Ålesund |
| Pyranometer | CMP22 | 200-3600 | Total and diffuse solar flux | 1 min | Ny-Ålesund |
| Pyrgeometer | PIR | 4000-50000 | Infrared flux | 1 min | Ny-Ålesund |

Table 2. Daily means of aerosol single scattering albedo (SSA), Angstrom Exponent (AE; 440/869 nm), Absorbing Angstrom Exponent (AAE; 441/869 nm), asymmetry parameter, refractive index and effective radius retrieved from CIMEL measured in Hornsund (AERONET lev. 2.0) and Andenes (AERONET lev. 1.5). Optical properties are given at 441 and 869 nm (the last value in the parentheses).

| Station | Data | SSA | AE | AAE | Asymm. parameter | Refractive index | | Effective radius [μm] |
|---|---|---|---|---|---|---|---|---|
| | | | | | | real | imaginary | |
| Hornsund | 10-07-2015 | 0.98 (0.97) | 1.59 | 1.14 | 0.70 (0.54) | 1.35 (1.42) | 0.0027 (0.0027) | 0.15 |
| | 12-07-2015 | 0.99 (0.99) | 1.50 | 1.25 | 0.70 (0.57) | 1.49 (1.53) | 0.0011 (0.0011) | 0.20 |
| Andenes | 12-07-2015 | 0.94 (0.91) | 1.51 | 1.02 | 0.70 (0.60) | 1.54 (1.50) | 0.011 (0.014) | 0.23 |
| | 13-07-2015 | 0.93 (0.90) | 1.46 | 1.03 | 0.70 (0.61) | 1.53 (1.50) | 0.013 (0.016) | 0.24 |